The Climate Impact of Hydrogen Powered Hypersonic Transport

Johannes Pletzer[1,2], Didier Hauglustaine[3], Yann Cohen[3], Patrick Jöckel[1], and Volker Grewe[1,2]

[1]Deutsches Zentrum für Luft- und Raumfahrt, Institut für Physik der Atmosphäre, Oberpfaffenhofen, Germany
[2]Delft University of Technology, Kluyverweg 1, 2629 HS Delft, The Netherlands
[3]Laboratoire des Sciences du Climat et de l'Environnement, LSCE-IPSL (CEA-CNRS-UVSQ), Université Paris-Saclay, 91191 Gif-sur-Yvette, France

Correspondence: Johannes Pletzer (johannes.pletzer@dlr.de)

Abstract. Hypersonic aircraft flying at Mach 5 to 8 are a means for travelling very long distances in extremely short times and even significantly faster than supersonic transport (Mach 1.5 to 2.5). Fueled with liquid hydrogen (LH2) their emissions consist of water vapour (H_2O), nitrogen oxides (NO_x) and unburnt hydrogen. If LH2 is produced in a climate- and carbon neutral manner, carbon dioxide does not have to be included when calculating the climate footprint. H_2O that is emitted near the surface has a very short residence time (hours) and thereby no considerable climate impact. Super- and hypersonic aviation emit at very high altitudes (15 km to 35 km) and H_2O residence times increase with altitude from months to several years with large latitudinal variations. Therefore, emitted H_2O has a substantial impact on climate via high altitude H_2O changes. Since the (photo-)chemical lifetime of H_2O is largely decreasing at altitudes above 30 km via the reaction with $O(^1D)$ and via photolysis, the question is whether the H_2O climate impact from hypersonics flying above 30 km becomes smaller with higher cruise altitude. Here we use two state-of-the-art chemistry-climate models and a climate response model to investigate atmospheric changes and respective climate impacts due to two potential hypersonic fleets flying at 26 km and 35 km, respectively. We show for the first time that the (photo-)chemical H_2O depletion of H_2O emissions at these altitudes is overcompensated by a recombination of hydroxyl radicals to H_2O and an enhanced methane and nitric acid depletion. These processes lead to an increase in H_2O concentrations compared to a case with no emissions from hypersonic aircraft. This results in a steady increase with altitude of the H_2O perturbation lifetime of up to 4.41 ± 0.20 years at 35 km. We find a 18.2 ± 2.8 mW m^{-2} and 36.9 ± 3.41 mW m^{-2} increase in stratosphere adjusted radiative forcing due to the two hypersonic fleets flying at 26 km and 35 km respectively. Ozone changes contribute 8-22 % and water vapour changes contribute 78-92 % to the warming on average. Our calculations show that the climate impact, i.e. mean-surface temperature change derived from the stratosphere adjusted radiative forcing, of hypersonic transport is estimated to be roughly 8-20 times larger than a subsonic reference aircraft with the same transport volume (revenue passenger kilometers) and that the main contribution stems from H_2O.

1 Introduction

The climate impact of aircraft emissions has been studied for decades and becomes more and more important. Estimated aviation growth rates will increase aviation's contribution to climate change and by that challenge the support of the Paris

25 Climate Agreement (UN, 2015; Terrenoire et al., 2019; Grewe et al., 2021, Planes et al., 2021). A recent study estimates the contribution of aircraft activity to human-made climate change to 3.5 (3.4, 4.0) %, which is an estimate based on effective radiative forcing and aviation fuel use (2011) (Lee et al., 2021). Furthermore, while carbon dioxide (CO_2) effects contribute one-third to the effective radiative forcing, non-CO_2 effects contribute two-thirds. This estimate is based on current aircraft fleets that are powered with kerosene and fly at altitudes from 10 to 12 km. With these aircraft, it takes travellers approximately

30 one day to fly around the world.

Two development goals for future aircraft fleets are on one hand to reduce climate impact and on the other hand to reduce travel time. As an example, roadmaps for a more climate-friendly liquid-hydrogen based aviation industry have been developed in agreement with existing research and estimate the potential reduction in climate impact to be 50-75 % (Fuel Cells and Hydrogen: Joint Undertaking, 2020). But this mainly addresses the concept of subsonic aircraft flying at 10-12 km alti-

35 tude. Higher altitudes are especially interesting for high-speed aircraft concepts that promise customers to save a considerable amount of travel time, especially on middle- and long-range flights. Aircraft designs in that category are super- and hypersonic aircraft. These aircraft are designed to travel at higher speed and higher altitudes compared to conventional subsonic aircraft and could reduce travel time around the globe to some hours. In turn, however, flight altitude and fuel type, which depend on aircraft design, can have a strong influence on atmospheric composition and thus on climate impact. The climate impact of

40 high-speed aircraft designs has been addressed for supersonic aircraft flying in the lower stratosphere with kerosene as well as with cryogenic fuels (IPCC, 1999; Gauss et al., 2003; Grewe et al., 2007, 2010).

Impact of supersonic aircraft at stratospheric altitudes is often discussed in terms of ozone concentration changes and ultra-violet radiation and extensive overviews on these topics have recently been published (Zhang et al., 2021; Tuck, 2021; Matthes et al., 2022). The first notes, that NO_x from supersonics might significantly affect the ozone layer were published in the 1970s

45 (Crutzen, 1970, 1972; Johnston, 1971). Additionally, there are multiple publications on the quantitative climate impact of supersonic aircraft fleets. A review of a selection of research programs including a direct comparison of radiative forcings (RF) was given by Grewe et al. (2010), who estimated the ratio of RF from supersonic to subsonic aircraft to be 3 (S4TA fleet, eight passengers), 6 (Airbus fleet, 250 passengers, Grewe et al. (2007)) and 14 (Boeing fleet, 309 passengers, IPCC (1999)). While these numbers initially appear to differ greatly, the authors present a correlation of flight altitude (range from 15-20 km) and RF

50 of non-CO_2 effects and additionally state that supersonic climate impact can approximately be scaled with fuel consumption. Hence, cruise altitude (i.e. speed which in turn influences fuel consumption) clearly is a crucial factor for climate impact.

At even higher altitudes, in the middle to upper stratosphere, hypersonic aircraft travel at MACH 4 or more and the emitted trace gases are reacting in another atmospheric environment compared to sub- and supersonic aircraft. Depending on cruise altitude and latitude of potential routes, hypersonic aircraft could fly in the upper parts of or above the ozone layer. As reference,

55 the ozone (O_3) mixing ratio is largest at around 31 km at tropical regions and has no clear peak at polar regions (Tegtmeier et al., 2013). The middle atmospheric balance of water vapour is determined by methane oxidation, photochemical lifetimes of HO_x compounds and upward transport through the tropical upper troposphere–lower stratosphere (UTLS), which is limited by the cold temperatures (Brasseur and Solomon, 2005; Frank et al., 2018; le Texier et al., 1988). Polar dehydration caused by the sedimentation of polar stratospheric cloud particles contributes to the balance. The climate impact of hypersonic aircraft

emissions is largely depending on their atmospheric residence time. More specifically, the residence time of species emitted by aircraft in the stratosphere is mainly controlled by the large-scale circulation of air (Brewer-Dobson circulation), their chemical interaction with stratospheric air constituents and photolysis. All three processes are highly dependent on altitude. The amount of emitted species is determined by aircraft and engine design, fuel type and trajectory layout. Kerosene, as the conventional fuel, is a technical option for hypersonic aircraft, but the initial focus in hypersonic studies is often on cryogenic aircraft. In general, cryogenic aircraft can be powered by pure gases such as methane (CH_4) or hydrogen (H_2) that are cooled to the liquid phase with the goal of reducing volume, i.e. increasing range per tank fill, and for other technical advantages (Peschka, 1998). Hence, compared to kerosene, cryogenic fuel could in theory be particle-free and would not have an indirect aerosol effect (Ponater et al., 2006). One of the few potential cryogenic fuels is liquid natural gas (LNG), which consists mostly of CH_4. Similar to kerosene-fueled aircraft, LNG ultimately increases atmospheric CO_2 concentrations. In comparison to H_2 fuel, LNG's direct climate impact could be slightly lower at specific altitudes (Grewe et al., 2017, cruise altitude approximately 13 km). However, the CO_2 perturbation originating from fossil fuel is subject to a large variety of sinks with different lifetimes. In general, the range is approximated with 2-20 centuries, where most of the CO_2 is taken up by ocean and biosphere sinks and 20-35 % remain in the atmosphere for longer time. Hence, released CO_2 will affect climate for tens of thousands to hundreds of thousands of years (Archer and Brovkin, 2008; Archer et al., 2009). On the other hand, H_2 fueled aircraft emit mainly water vapor (H_2O), whereas nitrogen oxides (NO_x) and H_2 are byproducts, with the latter depending on combustion efficiency. Their lifetimes are hours to years for H_2O and years for NO_x and H_2 (Brasseur and Solomon, 2005; Johnston et al., 1989; Grewe and Stenke, 2008; Ehhalt and Rohrer, 2009), which is substantially lower than for CO_2. Hence, a lifetime at least an order of magnitude shorter is a reason why currently H_2 fuel is often the preferred climate-friendly option for hypersonic aircraft designs. Another reason is the potentially more efficient (photo-)chemical destruction of H_2O at high altitudes, reducing the residence time and thus climate impact of emitted H_2O. More specifically, several studies suggest that chemical reaction of H_2O with $O(^1D)$ and photolysis could efficiently remove emitted H_2O at upper stratospheric altitudes and higher (Brasseur and Solomon, 2005; Steelant et al., 2015). This could potentially create a synergy of aircraft flying at these altitudes and H_2 propulsion aimed at reducing climate impacts. Thus, hypersonic aircraft with H_2 propulsion are seen as a potentially more climate friendly alternative to supersonic aircraft. For completeness, it is important to mention that the choice of fuel type does not only include climate impact, but is a trade-off between, for example, energy content, i.e. best range of aircraft, or cooling properties for thermal regulation (Blanvillain and Gallic, 2015).

However, the quantitative climate impact of hypersonic aircraft, regardless of fuel type, has not yet been assessed with a global atmospheric model and how it compares to supersonic aircraft still remains as well to be answered. Especially H_2 fueled aircraft are important to look at due to the broad discussions about global H_2 infrastructure and in consideration of the fact that H_2O is a potent greenhouse gas that affects ozone at stratospheric altitudes (Stenke and Grewe, 2005). Recent publications on the impact on atmospheric composition by hypersonic aircraft are few and focus on H_2 fueled aircraft. Ingenito (2018) published an estimate based on a fleet of 200 aircraft of type LAPCAT II MR2.4 (Steelant and Langener, 2014, Long-Term Advanced Propulsion Concepts and Technologies) flying at 30 km altitude, quantifying the reduction of atmospheric ozone with $3.6 \ 10^{-4}$ % and a temperature increase due to H_2O to 142 mK in one year. Another study by Kinnison et al. (2020)

was done with a global atmospheric model to assess the impact of hypersonic fleet emissions on the ozone layer at 30 and 40 km altitude. They focus on the sensitivity of stratospheric ozone to local perturbations of NO_x and H_2O. Their estimate for a reduction of atmospheric ozone with the same amount of fuel is 4.0 % and 2.2 % at 30 km and 40 km, respectively.

In this study we evaluate the climate impact of non-CO_2 effects from hypersonic aircraft and its altitude dependency with the metric stratosphere adjusted RF. In particular, we present the impact of H_2O, NO_x and H_2 emissions by hypersonic aircraft driven with H_2 fuel on atmospheric composition and briefly discuss the change in UV radiation. The results are based on the comparison of simulations with two chemistry climate models. The hypersonic emission data this study is using, was developed in the 'HIgh speed Key technologies for future Air transport - Research & Innovation cooperation scheme'-project (HIKARI, Blanvillain and Gallic (2015)), whose authors recommend H_2 fuel as a first choice. The economic and technical requirements of two fleets of hypersonic aircraft considered there will provide the estimate of the altitude dependency of climate impact of hypersonic aircraft emissions. Two advanced hypersonic fleet scenarios (Technology Readiness Level 1-3), differing in cruise altitude, cruise speed and thus fuel consumption, will allow the comparison of climate impacts of technically viable hypersonic aircraft concepts. The two hypersonic aircraft designs considered here are the models ZEHST (Zero Emission High-Speed Transport) and LAPCAT PREPHA-type (Falempin et al., 1998; Scherrer et al., 2016, Programme de REcherche et de technologie sur la Propulsion Hypersonique Avancée) with cruise altitude at approximately 26 km and 35 km, respectively. The paper is structured as follows. After the introduction, we present the two chemistry-climate models EMAC (ECHAM/MESSy; European Centre HAMburg general circulation model; Modular Earth Submodel System) and LMDZ-INCA (Laboratoire de Météorologie Dynamique; INteraction with Chemistry and Aerosols) and their setups. In Sect. 3 we present the HIKARI emission inventory and the temporal evolution of aircraft emissions. After a model evaluation with aircraft measurements in Sect. 4, we show the atmospheric composition changes in Sect. 5. The climate impact is part of Sect. 6 'Radiation and Climate'. In the end, a discussion and summary is included.

2 Methods and Simulations

We have performed simulations of atmospheric changes caused by emissions from hypersonic transport with the two Atmospheric Chemistry General Circulation Models (AC-GCMs) EMAC and LMDZ-INCA in order to address model dependencies of the results. Differences and conformity between model setups that were used in this study are presented in Table 1. It lists the key properties of both models. EMAC consists of the spectral dynamical core of the GCM ECHAM5 by the Max Planck-Institute for Meteorology (Roeckner et al., 2006, version five) and MESSy, able to combine all components relevant for Earth System Models, published by Jöckel et al. (2005, 2010, 2016).

The LMDZ-INCA global chemistry-aerosol-climate model couples on-line the LMDZ General Circulation Model (version six, Hourdin et al., 2020) and the INCA model (version five, Hauglustaine et al., 2004; 2014). The interaction between the atmosphere and the land surface is ensured through the coupling of LMDZ with the ORCHIDEE (ORganizing Carbon and Hydrology In Dynamic Ecosystems, version 1.9) dynamical vegetation model (Krinner et al., 2005). More information on the model set-ups are presented in the following sub-chapters.

Table 1. Table stating the key properties of model setups for EMAC and LMDZ-INCA as applied for this study.

Model	EMAC[1]	LMDZ-INCA
GCM	ECHAM	LMDZ
Vertical limits [km]	0-80	0-80
Vertical limits [hPa]	Surface-0.01	Surface-0.04
Nudging limits [hPa]	Surface-10.0	Surface-1.0
Nudging data	ERA-Interim	ERA-Interim
Nudging relax. time	6-48 hrs	2.5 hrs
Grid cells (lon,lat,lev)	128 x 64 x 90[2]	144 x 143 x 39

[1]ECHAM5 v5.3.02, MESSy v2.54.0, Jöckel et al. (2010). [2]Named T42L90MA where T42 refers to a triangular truncation at wave number 42, corresponding to a quadratic Gaussian grid of approximately 2.8 ° by 2.8 ° in latitude and longitude, L90 refers to 90 vertical hybrid pressure levels and MA to 'Middle Atmosphere'.

While the model setups of EMAC and LMDZ-INCA are consistent with respect to the model domain and nudging data there are differences with respect to the vertical resolution, the nudging relaxation time and the model domain where nudging is applied. Both models were intensively validated, e.g. the dynamics at stratospheric altitudes by the model's stratospheric age of air and by tropical upward mass flux. Further details on the respective models are given in the following subsections.

2.1 EMAC Model Set-Up

The EMAC model setup is based on that of simulation RC1SD-base-10, recommended due to it's affirmative agreement with observations, especially ozone, and described in detail by Jöckel et al. (2016). The vertical resolution of the 90 hybrid model layers in EMAC is approximately 550 m in the UTLS region, reaches 1200 m at the stratopause and increases to 3200 m in the middle atmosphere The model results were compared extensively with ERA-Interim. Deviations from model to observations are a cold bias with a vertical maximum at 200 hPa and values of $\pm$ 4 K (Fig. 12, Jöckel et al. (2016)). A comparison with satellite data shows that over the annual cycle ozone volume mixing ratios are well reproduced in the stratosphere, apart from southern polar regions and with larger differences at tropospheric altitudes. The stratospheric southern polar bias is larger in free running EMAC simulations and especially low in simulations with specified dynamics (without mean temperature nudging). Hence, our chosen EMAC model setup is especially well suited for our application of modelling stratospheric ozone. An IAGOS-CARIBIC (In-service Aircraft for a Global Observing System; Civil Aircraft for the Regular Investigation of the atmosphere Based on an Instrument Container: Petzold et al., 2015) data comparison for the UTLS shows deviations around 5 % and larger values up to 30 % in June-September for regions above the tropopause and an overestimate of up to 40 % in the troposphere. Methane, carbon monoxide and acetone concentrations are underestimated by the model, specifically at tropospheric altitudes. Transport by the Brewer-Dobson-Circulation was tested by comparing the model tropical upward mass flux to ERA-Interim and mean age of stratospheric air (AoA) to MIPAS (Michelson Interferometer for Passive Atmospheric Sounding) observations. While the largest differences for AoA are at polar latitudes and the upper stratosphere, the model still shows overall a reasonable agreement, especially for the lower stratosphere and extratropics, and the tropical upward mass flux shows the best agreement for setups with specified dynamics (nudging) and without global mean temperature nudging (Jöckel et al., 2016). Summarizing, while there are deviations, the setup including nudging is among the others especially well suited for stratospheric sensitivity studies.

As this study assesses the impact of emitted H_2O (as well as NO_x and H_2), a decoupling of atmospheric dynamic, chemistry and radiation was technically not possible when adding H_2O to the model's hydrological cycle. However, we achieved a sufficiently large signal-to-noise ratio by Newtonian relaxation (nudging) towards ERA-Interim reanalysis data for the years 2000-2014. EMAC is based on the spectral transform dynamical core of ECHAM. The nudging is applied by Newtonian relaxation of the prognostic variables divergence, vorticity, temperature and the logarithm of the surface pressure in the spectral representation (spherical harmonics) of these variables towards the ECMWF (European Centre for Medium-Range Weather Forecasts) ERA-5 reanalysis data (Dee et al., 2011). u and v wind are derived variables calculated through derivation and spectral transformation. The wave-0 of temperature (global mean) is omitted, there is further no nudging applied on the sub-synoptic scale, aiming at an optimal compromise between observed (i.e. reanalysed) and simulated meteorology. Moreover, the nudging is applied in vertical direction only between the 4th model layer above the ground and approximately 200 hPa, in order to avoid inconsistencies in the planetary boundary layer and to let the stratosphere develop freely and driven by the tropospheric wave activity. This nudging setup is identical to that of the RC1SD-base-10 simulation described by Jöckel et al. (2016). The ECMWF ERA-5 reanalysis data are preprocessed by spectral transformation and truncation for the applied model resolution.

The respective relaxation times are listed in Table 1. Further information on the very similar nudging process, apart from different relaxation times, is described in the next subsection about LMDZ-INCA. Prognostic variables were accounted for by the MESSy submodel TENDENCY to tag submodel contributions like e.g. cloud-, advection- or emission-processes to specific humidity (Eichinger and Jöckel, 2014). Additionally, H_2O emissions were added to the model's hydrological cycle with a new MESSy submodel (H2OEMIS), which uses either TENDENCY (in this study) or directly adds water vapour perturbations to the specific humidity tracer. An overview of all active submodels can be found in the appendix.

2.1.1 ECHAM5/MESSy Submodel H2OEMIS

H_2O and the associated hydrological cycle play an important role in atmospheric radiation and dynamics and thereby the general circulation. As it is a precursor of the atmospheric hydroxyl radical (OH), it also largely controls atmospheric chemistry. For earlier versions of the model, the chemistry calculations were operated with an H_2O-tracer that had to be kept synchronous with the prognostic specific humidity of the underlying GCM. In recent versions, the chemistry feedback on the hydrological cycle now directly alters the specific humidity. Due to this it was not possible to include offline H_2O to alter the prognostic specific humidity directly. But the modular structure easily allowed the development of the new submodel H2OEMIS to include the possibility to directly emit H_2O into the atmosphere and alter specific humidity. Briefly summarized, gridded H_2O emission flux data is imported into the model via the IMPORT submodel (Kerkweg and Jöckel, 2015), then H2OEMIS converts the flux into a tendency of the specific humidity and applies this tendency to the prognostic variable qm1, i.e. specific humidity in MESSy. The submodel and further information are available with the MESSy release version 2.55.0. Two short movies can be found in the video supplements showing emitted H_2O by hypersonic aircraft and it's addition to the specific humidity (zonal mean representation and world map view respectively).

2.1.2 Additional Diagnosis of Chemical Destruction and Production of H_2O with MECCA

The net amount of chemical production and destruction of H_2O is significant for the concentration of H_2O in the stratosphere. Above 20 km the largest contribution comes from transport through the tropical tropopause layer via the deep branch of the Brewer-Dobson-Circulation and oxidation of CH_4, which was recently reconfirmed with EMAC model studies by Eichinger et al. (2015a, b); Frank et al. (2018) and satellite studies by Noël et al. (2018). In EMAC the chemical mechanism is applied among others via the MESSy submodel MECCA (Module Efficiently Calculating the Chemistry of the Atmosphere) developed by Sander et al. (2005, 2011). This specific submodel is able to include tracers that keep track of production as well as destruction of chemical reactants. Thus we included five tracers for chemical destruction of H_2O and 45 tracers for chemical production of H_2O for a deeper understanding of underlying processes. Further information on the H_2O-specific reaction rates and all other reaction rates are given in the supplement of this study (file *meccanism.pdf, scavinism.pdf*) and beyond that in the supplement of Jöckel et al. (2016). While MECCA considers gas- and heterogeneous-phase reactions in the tropo- and stratosphere, the submodel SCAV (SCAVenging) includes aqueous phase reactions in clouds and precipitation and the corresponding induced removal of trace gases and aerosols by wet deposition (Tost et al., 2006), CH4 (Winterstein and Jöckel, 2021) issues CH_4 oxidation (while MECCA feedbacks to specific humidity), MSBM (Multiphase Stratospheric Box Model)

calculates the polar stratospheric cloud-chemistry (Jöckel et al., 2010), DDEP (Dry DEPosition) and SEDI (SEDImentation)
are responsible for dry deposition and sedimentation of aerosols, respectively (Kerkweg et al., 2006a), AIRSEA addresses air
and ocean surface interaction (Pozzer et al., 2006), OFFEMIS (OFFline EMISsion) and ONEMIS (ONline EMISsion) add
prescribed and online-calculated emissions (Kerkweg et al., 2006b) and LNOX (Lightning Nitrogen OXides) includes NO_x
production by lightning, where we used the 'Grewe' coupling parameterisation as described in Tost et al. (2007); Grewe et al.
(2001), which is based on convective mass-flux. The resulting total lightning NO_x for the baseline simulation is 5.0 TgN/yr.

2.2 LMDZ-INCA Model Set-Up

In the present LMDZ-INCA configuration, we use the "Standard Physics" parameterization of the GCM (Boucher et al., 2020).
The model includes 39 hybrid vertical levels extending from the surface up to 80 km. The vertical resolution of LMDZ-INCA
in the applied resolution is approximately 1000-1300 m in the UTLS region, reaches 5000 m at the stratopause and increases
to 8700 m in the mesosphere. The horizontal resolution is 1.9 degrees in latitude and 3.75 degrees in longitude. The primitive
equations in the GCM are solved with a 3 min time-step, large-scale transport of tracers is carried out every 15 min, and physical
and chemical processes are calculated at a 30 min time interval. For a more detailed description and an extended evaluation
of the GCM we refer to Hourdin et al. (2020). The large-scale advection of tracers is calculated based on a monotonic finite-
volume second-order scheme (Hourdin and Armengaud 1999). Deep convection is parameterized according to the scheme of
Emanuel (1991). The turbulent mixing in the planetary boundary layer is based on a local second-order closure formalism. The
transport and mixing of tracers in the LMDZ GCM have been investigated and evaluated against observations for both inert
tracers and radioactive tracers (e.g., Hourdin and Issartel, 2000; Hauglustaine et al., 2004) and in the framework of inverse
modelling studies (e.g., Bousquet et al., 2010; Zhao et al., 2019).

INCA initially included a state-of-the-art $CH4-NO_x-CO-NMHC-O_3$ tropospheric photochemistry (Hauglustaine et al., 2004;
Folberth et al., 2006). The tropospheric photochemistry and aerosols scheme used in this model version is described through
a total of 123 tracers including 22 tracers to represent aerosols. The model includes 234 homogeneous chemical reactions, 43
photolytic reactions and 30 heterogeneous reactions. Please refer to Hauglustaine et al. (2004) and Folberth et al. (2006) for
the list of reactions included in the tropospheric chemistry scheme. The gas-phase version of the model has been extensively
compared to observations in the lower-troposphere and in the upper-troposphere. For aerosols, the INCA model simulates the
distribution of aerosols with anthropogenic sources such as sulfates, nitrates, black carbon (BC), organic carbon (OC), as well
as natural aerosols such as sea-salt and dust. The aerosol component of the LMDZ-INCA model has been extensively evaluated
during the various phases of AEROCOM (e.g., Gliss et al., 2021; Bian et al., 2017).

Earlier versions of the LMDZ-INCA model including gas phase tropospheric chemistry only have been previously used to
assess the impact of subsonic aircraft on tropospheric ozone (Koffi et al., 2010; Hauglustaine and Koffi, 2012). This version of
the model has been extended to include an interactive chemistry in the stratosphere and mesosphere (Terrenoire et al., 2022).
Chemical species and reactions specific to the middle atmosphere have been included in the model. A total of 31 species
were added to the standard chemical scheme, mostly belonging to the chlorine and bromine chemistry, and 66 gas phase
reactions and 26 photolytic reactions. Water vapor is now affected by both physical and chemical processes in LMDZ. In the

stratosphere, an additional tracer is introduced in order to account for photochemical production and destruction in INCA. In addition, heterogeneous processes on Polar Stratospheric Clouds (PSCs) and stratospheric aerosols are parameterized in INCA

235 following the scheme implemented by Lefevre et al. (1994). The excess of H_2O and HNO_3 is removed from the gas phase when saturation occurs and is used to compute the surface area concentration in the PSC region. Heterogeneous reaction rates are calculated explicitly, as a function of the surface area available, mean molecular velocity, and the reaction probabilities. The model does distinguish between liquid nitric acid trihydrate (NAT, $HNO3 \cdot 3\ H2O$), liquid supercooled ternary solutions (STS, $HNO3 \cdot H2SO4 \cdot H2O$) and solid ice PSCs. Furthermore, the PSC scheme includes sedimentation of the PSC particles which

240 affects the vertical distribution H_2O, HNO_3, and HCl. Condensed species are returned to the gas phase when clouds evaporate. In the presence of PSCs, the heterogeneous reactions convert bromine and chlorine reservoirs (HCl, HBr, $ClONO_2$, $BrONO_2$) into reactive species (Cl_2, $ClNO_2$, HOCl, Br_2, $BrNO_2$, HOBr) based on 9 additional heterogeneous reactions introduced in the chemical scheme. The distribution of stratospheric aerosols is prescribed according to the CCMI exercise (Chemistry-Climate Model Initiative, Thomason et al., 2018).

245 In this study, meteorological data from the European Center for Medium-Range Weather Forecasts (ECMWF) ERA-Interim reanalysis have been used to nudge the GCM winds from 1000 - 1 hPa. These GCM winds are interpolated on the horizontal grid before the simulation runs and are interpolated on the model pressure levels at each time step. The relaxation of the GCM winds towards ECMWF meteorology is performed by applying at each time step a correction term to the GCM u and v wind components with a relaxation time of 2.5 hours (Hourdin and Issartel, 2000; Hauglustaine et al., 2004). The ECMWF fields

250 are provided every 6 hours and interpolated onto the LMDZ grid.

The anthropogenic emissions from the Shared Socioeconomic Pathways scenarios (SSPs) (scenario SSP3-7.0) prepared by Gidden et al. (2019) are used and added to the natural fluxes used in the INCA model. The ORCHIDEE vegetation model has been used to calculate off-line the biogenic surface fluxes of isoprene, terpenes, acetone and methanol as well as NO soil emissions as described by Lathière et al. (2006). The lightning NO_x emissions are parameterized in the model based

255 on convective cloud heights as described in Jourdain et al. (2001). Based on this parameterization, the total lightning NO_x emissions for the baseline simulation is 5.5 TgN/yr.

2.3 Simulations

Both models simulate a time period of fifteen years. This includes a ten to twelve year spin-up phase to achieve a chemical and dynamic equilibrium that takes into account long lifetimes of trace gases in the stratosphere. Lower boundary conditions, direct-

260 and traffic-emissions of simulations are based on IPCC's (Intergovernmental Panel on Climate Change) RCP6.0 (Relative Concentration Pathway) scenario (CCMI) for EMAC and the SSP3-7.0 (Shared Socioeconomic Pathways) scenario for LMDZ-INCA. This includes the surface mixing ratios for methane, nitrous oxide as well as chlorine and bromine containing species and excludes air traffic, where we used an emission inventory from the HIKARI project. The RCP6.0 and SSP3-7.0 scenarios are very similar and the latter can be treated as an updated version (from the Coupled Model Intercomparison Project (CMIP)

265 Phase 6) of the former (from CMIP Phase 5). The beginning of air fleet operation including hypersonic aircraft was set to 2050. Therefore, the assumptions of the RCP scenario for other emissions are the fifteen year period 2050-2064. The assumptions of

SSP are fixed on their 2050 values. In summary, on one hand, the simulations were carried out with nudged dynamics allowing a reduction of the signal-to-noise ratio from the time period 2000-2014, and, on the other hand, the atmosphere's chemical composition of simulations is based on assumptions from 2050 (and onwards) i.e. when hypersonic aircraft technology is potentially ready for commercial use.

270

3 The HIKARI Emission Inventory and Spin Up

3.1 Emission

HIKARI was an international project of Europe and Japan for high-speed transport resulting in a potential timeline for further development of high-speed transportation up to commercial operation (Hikari means 'Light' in japanese, 2015). Blanvillain and Gallic published the roadmap study in 2015, which combines economic viability, environmental constraints as well as technological requirements. We use the formerly unpublished trade-off emission scenarios by HIKARI. These include two hypersonic scenarios with aircraft ZEHST and LAPCAT.

- ZEHST is short for Zero Emission High-Speed Transport and is a high-speed aircraft project, which includes a strategy to reduce environmental impact with a zero CO_2 emission policy. The aircraft is based on a ramjet engine for cruise phase and travelling speed is at Mach 4-5. This aircraft is developed for 60 passengers and an intermediate transport range of approximately 9 000 km (e.g. Paris-Tokyo, Defoort et al. (2012)).

- LAPCAT is short for Long-Term Advanced Propulsion Concepts and Technologies. It is a joint effort of many European institutes, resulting among others in an aircraft model meant to travel at Mach 8 with scramjet technology, carry up to 300 passengers and for long-range flights of approximately 18 000 km (e.g. Brussels-Sydney, Steelant and Langener (2014); Steelant et al. (2015)). The LAPCAT version is based on the technology level developed in the French high speed propulsion program PREPHA.
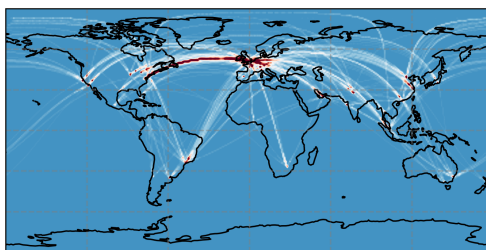

Figure 1. World map of H_2O emission location (white to red) by LAPCAT aircraft summed over all vertical levels. A colorbar is not included because the motivation is to depict specifically the emission location. Only one plot representative for all HIKARI emission scenarios is shown, because hypersonic features of emission are dominant in the vertical sum and ZEHST and LAPCAT scenarios show a quite similar horizontal distribution on the world map. A vertical distribution is shown in Fig. 2.

While we focus on H_2 driven aircraft in this study, the HIKARI emission inventory includes carbon-based emission data as well. In general, H_2 driven aircraft with air-breathing engines emit H_2O and NO_x, but potentially includes a rest of unburnt H_2 fuel. For the HIKARI emission inventory 10 % of unburnt H_2 is assumed.

290   In total, the HIKARI emission inventory contains three scenarios. In addition to the subsonic reference scenario based on an Airbus A350, a mixed-fleet scenario with ZEHST-type hypersonic aircraft and a mixed-fleet scenario with LAPCAT-type hypersonic aircraft are part of this inventory (Fig. 2). The respective cruise altitudes are approximately 12, 26 and 35 km. All aircraft designs travel from and to the same city pairs. The horizontal resolution is 1° x 1° and the vertical resolution is 304.8 m.

295   The collection of annual emissions of trace gases for the three scenarios are listed in Table 2. This includes the global emissions as well as the proportion emitted at stratospheric altitudes and the latter mostly consists of trace gases emitted at the cruise phase of hypersonic aircraft. Approximately two-thirds of H_2O are emitted at stratospheric altitudes for both, the ZEHST and LAPCAT scenario, and one-third in the troposphere. The main part of NO_x is emitted at tropospheric altitudes and H_2 is emitted to 76 % and more at stratospheric altitudes. Another property shown in the same table, market penetration,

300   is a measure of how many of the global flight routes are suited for the specific hypersonic aircraft compared to subsonic aircraft. Hence, there is a smaller market for the aircraft LAPCAT whose design is able to travel extremely large distances (approximately 18,000 km) due to the limited selection of appropriate city pairs like Brussels-Sydney. In comparison, ZEHST is a potential faster alternative for 25 % of the subsonic aviation market with a smaller range (approximately 9,000 km). The aircraft designs differ in passenger seats with 60 for ZEHST and 300 for LAPCAT. In Fig. 2 (b) and (c) emission features at

305   altitudes 6-11 km are visible. This originates from acceleration and climb to cruise altitude by hypersonic aircraft of ZEHST and LAPCAT.
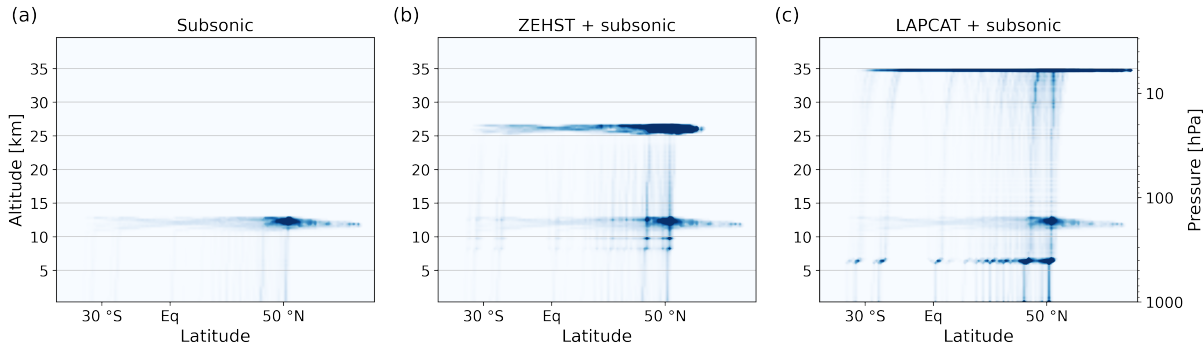

Figure 2. Zonal sum of trace gas emission location. (a) Depicts the subsonic reference scenario, (b) depicts the ZEHST scenario with a hypersonic market penetration of 9.8 % and (c) depicts the LAPCAT scenario with a hypersonic market penetration of 26.0 %. A colorbar with units is not shown, since the location (altitude, latitude) is the interesting piece of information here. For annual amounts of emissions see Table 2. The data is taken from the HIKARI project's emission inventory.

Table 2. HIKARI emission inventory. Annual emission of trace gas species H_2O, NO_x and H_2. The upper three rows contain amounts of trace gases emitted in the whole atmosphere, while the lower three rows contain amounts of trace gases emitted at stratospheric altitudes only (above 100 hPa). Note that for ZEHST and LAPCAT a part of the subsonic aviation is replaced by hypersonic transport and hence the numbers depict whole air traffic scenarios.

Scenario	Domain	H_2O [Tg yr^{-1}]	NO_x [TgNO$_2$ yr^{-1}]	H_2 [Tg yr^{-1}]	Market penetration[3]
Subsonic	global	5.022	0.072	0.0	0 %
ZEHST	global	21.581	0.113	0.163	9.8 %
LAPCAT	global	31.366	0.115	0.307	26.0 %
Subsonic	above 18 km	0.0	0.0	0.0	-
ZEHST	above 18 km	13.741	0.020	0.153	-
LAPCAT	above 18 km	21.237	0.031	0.236	-

[4]Market penetration depicts the ratio of subsonic to hypersonic aviation market, where hypersonic aircraft take over some of the subsonic market.

3.2 Spin Up and Temporal Evolution

The respective full aircraft fleet is in operation for the total simulated time of fifteen years. Annual emissions accumulate over the years and perturbation of emitted trace gas concentration eventually reach equilibrium at the multi-annual mean after 8-10 years. The emissions are balanced by transport and loss to tropospheric altitudes as well as (photo-)chemical losses and production. Five years of simulation in equilibrium remain for average values and significance tests. The monthly-mean mass perturbation above the tropopause (WMO, 1957) is shown in Fig. 3 over the simulation timeline from 2000 to 2015. EMAC and LMDZ-INCA show similar patterns of monthly oscillations. The oscillations of the latter are smoother, which potentially is related to the lower vertical resolution or the feedback between atmospheric composition and radiation in EMAC.

After fifteen years of continuous operation of hypersonic fleets, the total emission of trace gases for ZEHST and LAPCAT scenarios at stratospheric altitudes are 206 Tg and 319 Tg of H_2O, 0.3 Tg and 0.5 TgNO$_2$ of NO_x and 2.3 Tg and 3.5 Tg of H_2, respectively. During the fifteen years, the emitted trace gases, while being chemically converted, are continuously transported to tropospheric altitudes and only parts of the total emitted trace gases remain as perturbation. More information on the equilibrium perturbation is presented in Sect. 5.
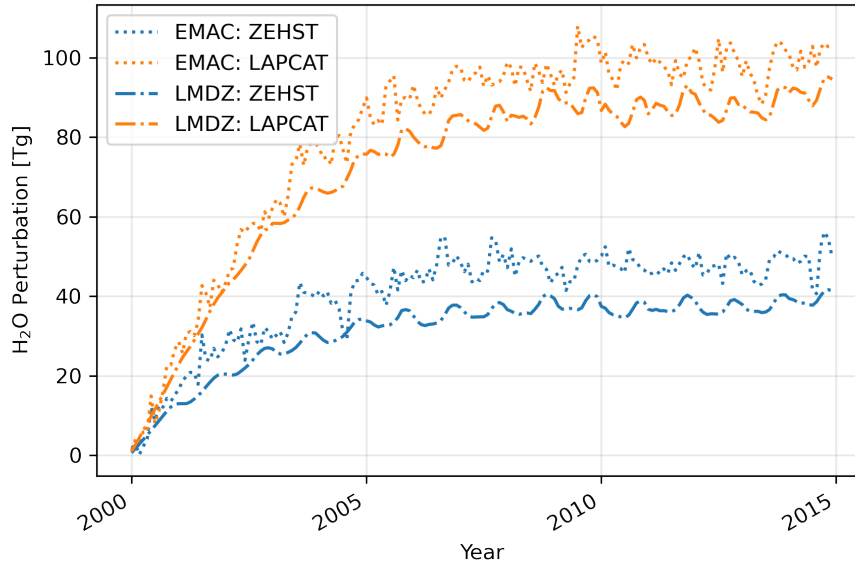
Figure 3. Temporal evolution of mass perturbation of H_2O in Tg above the tropopause. Blue and orange lines represent scenario ZEHST and LAPCAT, respectively. The annual amount of emitted trace gases is listed in Table 2.

4 Model Evaluation

In this chapter, we evaluate the model results with observations from commercial aircraft. It is important to verify the models performance in the upper troposphere–lower stratosphere region, especially in the northern extratropics, where most of the trace gases are emitted and the downward stratosphere-to-troposphere transport (SST) occurs. The SST, including the trace gases emitted at stratospheric altitudes, is a very important step of the continuous process, that eventually removes these trace gases from the atmosphere. A fact that is further emphasized by the results of this publication. IAGOS offers data particularly fit for this region of interest. In a forthcoming publication, we extend the evaluation to higher altitudes and compare EMAC model results to satellite data (Pletzer and Grewe, 2022, in prep). In addition, a comparison between LMDZ-INCA and ozone soundings measurements has also been presented in Terrenoire et al. (2022).

4.1 Observation data set

The research infrastructure IAGOS provides in situ measurements on board a fleet of commercial aircraft. Observations of ozone and water vapour started in August 1994 and are still being collected so far. IAGOS mostly samples the UTLS in the northern extratropics, with cruise data spreading between 9 and 12 km above sea level. The ozone instruments are based on UV-absorption spectrometry and their accuracy, precision and time response are 2 ppb, 2 % and 4 s, respectively. H_2O is measured using a capacitive hygrometer. The latter's precision and time response are generally 5 %, or 6 % in the thermal tropopause at

14

335 midlatitudes (Smit et al., 2014), for relative humidity and 5–300 s for H_2O, respectively, with regard to ice (Helten et al., 1998; Neis et al., 2015).

In order to allow a direct comparison between simulation outputs and the IAGOS data, the Interpol-IAGOS software (Cohen et al., 2021a) used here first projects observations onto model grids, then derives monthly means. The subsequent products are called IAGOS-DM-INCA and IAGOS-DM-EMAC. The -DM suffix refers to the distribution onto the model grid. Since

340 the output from the models have a daily resolution, a mask is applied with respect to the IAGOS sampling. The subsequent products are called INCA-M and EMAC-M. The -M suffix refers to the mask. In this way, the monthly means derived from both, the IAGOS and the simulations data sets, represent the same days for each grid cell.

Seasonal and annual climatologies are then calculated on the 3D models grids. As in Cohen et al. (2021a), a grid point is filtered out, if the total amount of IAGOS data is below a minimum threshold, the latter decreasing with latitudes in order to

345 account for the grid cell area. The validated grid points are then averaged together as partial columns, with a 400 hPa lower bound in order to exclude the IAGOS data recorded during ascent and descent phases near airports. In order to ensure a correct vertical representation, we select only the columns derived from at least two grid cells. Our assessment focuses on the northern midlatitudes since, first, the UTLS is far more influenced by the stratosphere in the extratropics than in the tropics and, second, only the UT is sampled in the tropics. The seasons defined in the northern midlatitudes are thus typically extratropical.

350 The scores used for the evaluation are the modified normalized mean bias (MNMB) and the Pearson correlation coefficient. For a set of N grid cells with an observed value o_i and a simulated value m_i, the MNMB is defined as follows:

$$MNMB = \frac{2}{N} \sum_{i=1}^{N} \frac{m_i - o_i}{m_i + o_i} \tag{1}$$

In contrast to the classical mean bias, that is sensitive to larger values, the MNMB treats large and small values with a similar sensitivity. Thus it is very valuable for an assessment in the UTLS without separating tropospheric and stratospheric air masses.

355 Indeed, since the tropopause altitude varies geographically, the aircraft fleet will record an important geographical variability in both, ozone and water vapour.

4.2 Model comparison to IAGOS observations

The evaluation of the simulations from EMAC and LMDZ-INCA against IAGOS in the northern extratropics are synthesized in the Taylor diagrams shown in Fig. 4, and in Figs. A7–**??** for the seasonal scale. They are derived from the mean climatologies

360 shown in Figs. A8–A12. Both model products are well correlated with the observations, with r $\sim$ 0.90 for water vapour in INCA-M, and r $\sim$ 0.95 in the other cases. Independent of the magnitude, the models capture the geographical variations well for ozone, water vapour and temperature. On annual average, the INCA-M product is characterized by a relatively weak mean bias in ozone, water vapour and temperature. The EMAC-M product has a systematic cold bias in the extra-tropics, with half of the grid cells ranging between -3.8 and -2.5 K. It leads to an upward shift of the tropopause and thereby underestimates

365 ozone and overestimates water vapour volume mixing ratios. These two features are visible in Fig. A8, where it is shown to be more representative of the higher latitudes. Last, according to Figs. A7–**??**, the ozone and water vapour biases keep
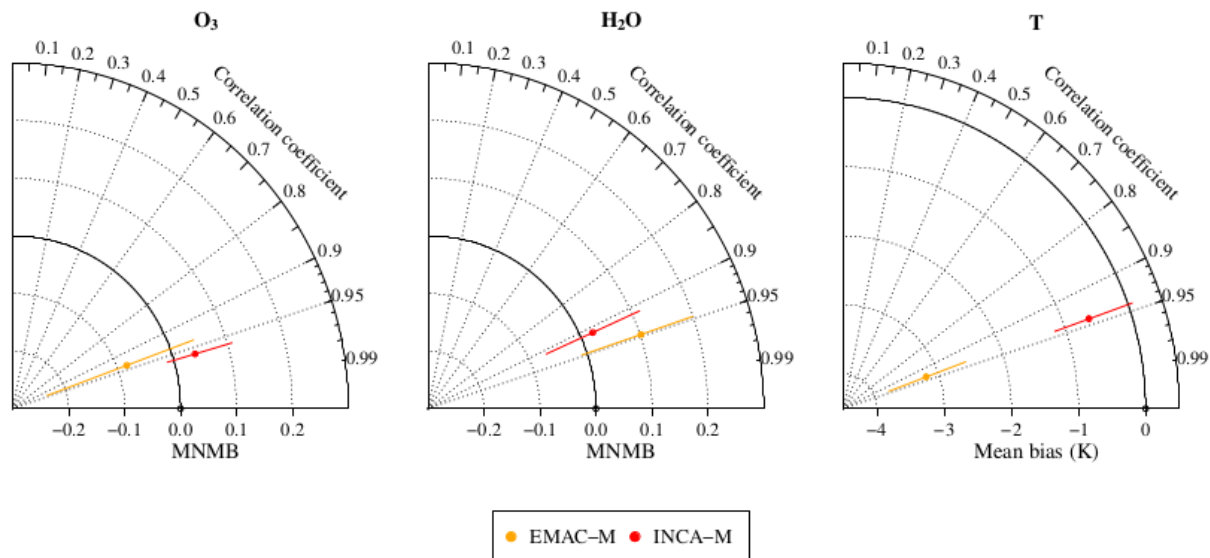
Figure 4. Taylor diagrams showing the assessment of the simulations against IAGOS in the northern extratropical UTLS. From left to right, ozone, water vapour and temperature are represented. For ozone and water vapour, the radial axis shows the modified normalized mean bias, and the mean bias for the temperature. The error bars represent the interquartile interval. The orthoradial axis displays the Pearson correlation coefficient.

the same sign through the seasons for EMAC-M, contrary to INCA-M. The ozone (respectively water vapour) MNMB are particularly negative (respectively positive) in both models during summer, possibly suggesting an increased underestimation of the stratospheric influence on the UTLS during this season.

5 Atmospheric Composition Changes

5.1 Water Vapour

Stratospheric water vapour (SWV) stems mostly from upward transport at tropical latitudes and oxidation of CH_4. The main factors for loss of SWV are reaction with $O(^1D)$, photolysis and the transport into the troposphere at the subtropical tropopause breaks. Additionally, polar stratospheric clouds cause dehydration through sedimentation of particles. Note that those processes are considered in our model simulations. Figure 5 shows the volume mixing ratio in equilibrium for the respective model and aircraft as a 5-year average (2010-2014). The SWV perturbation is clearly visible in both models, especially at the northern hemisphere with the maximum located at around 50-60° N, which overlaps with the maximum trace gas emission location. Overall, the perturbation patterns agree well between the models, especially for altitudes from 16 to 37 km (approximately 100-4 hPa) and with differences at higher altitudes 37 to 79 km (approximately 4-0.01 hPa). The latter altitude range contains only a small amount of the mass perturbation in the models, since the largest mass perturbation accumulates in the middle

16

and lower stratosphere, where air density is larger (Fig. A2, Fig. A3). A t-test shows that all zonal-mean H_2O perturbations are statistically significant at a 99.9 % level and only parts in the tropical UTLS (EMAC: ZEHST, LMDZ-INCA: ZEHST, LAPCAT) do not reach that value.
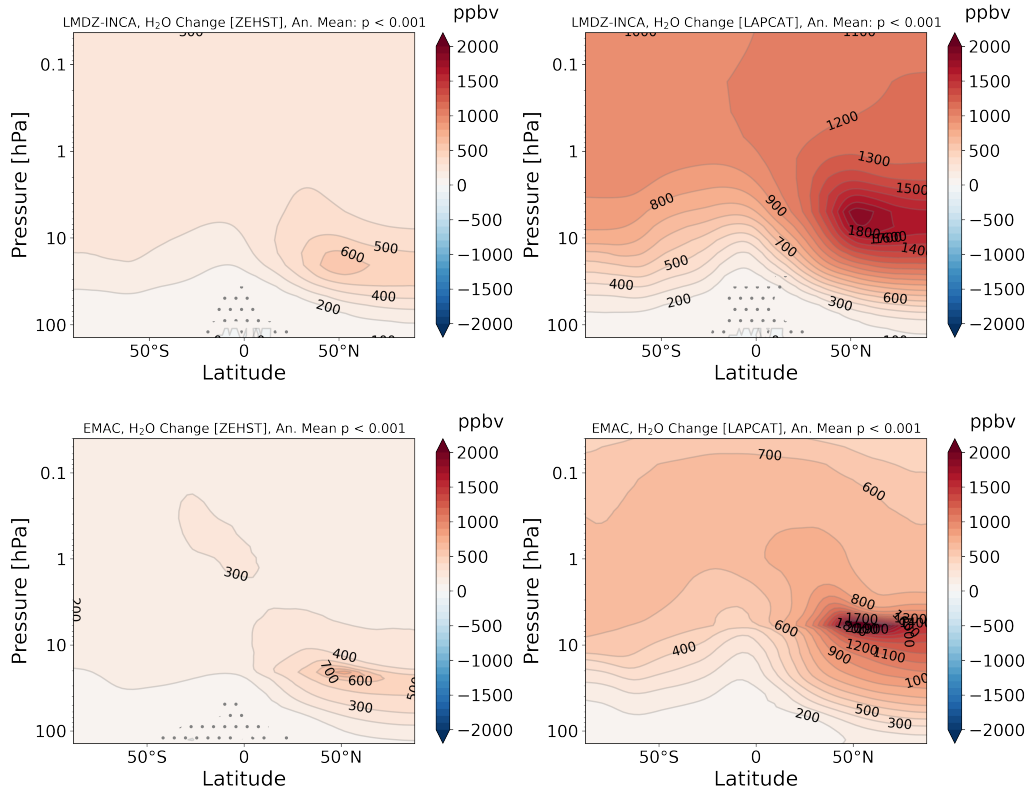

Figure 5. Multi-annual mean (2010-2014) of H_2O perturbations (ppbv) for the ZEHST scenario (left) and the LAPCAT scenario (right) for both models LMDZ-INCA (upper) and EMAC (lower) after approximately thirteen years of continuous emission. Cruise altitudes are approximately at the respective perturbation maxima. The dotted region corresponds to the grid points where the mean perturbations are not significant at a 99.9 % level.

Absolute values of the mass perturbation and the respective perturbation lifetime of water vapour are listed in Table 3. Values were calculated for the perturbation above the tropopause (WMO, 1957). The total H_2O mass perturbation is approximately twice as large for the higher flying aircraft compared to the lower flying aircraft for each model due to the longer transport to the troposphere and due to the larger emission. The perturbation lifetime clearly increases with cruise altitude from 2.8-3.5 years to 4.2-4.6 years. Due to the difference in annual H_2O emission of both aircraft, the perturbation lifetime scales differently compared to the mass perturbation.

Mass perturbation and perturbation lifetime are affected by the (photo-)chemical removal of emitted water vapour. The key processes are photolysis and reaction with $O(^1D)$. The combined average lifetime is shown in Fig. 6 for LMDZ-INCA (a) and

Table 3. Perturbation and perturbation lifetime of H_2O in teragram and years, respectively, for the ZEHST and the LAPCAT scenario and for each of the two models.

Model/Scenario	Perturb. ZEHST	Perturb. Lifetime ZEHST	Perturb. LAPCAT	Perturb. Lifetime LAPCAT
LMDZ-INCA	38.27 Tg	2.79 yr	89.45 Tg	4.21 yr
EMAC	47.82 Tg	3.50 yr	98.47 Tg	4.61 yr

EMAC (b). Photolysis clearly increases with altitude resulting in shortest lifetime at the upper end of the simulated altitude range and at the equator region, where incident sunlight is strongest on average. The reaction with $O(^1D)$ has a maximum at around 45-50 km, where the loss of O_3 due to photolysis and thus concentrations of excited atomic oxygen $O(^1D)$ is generally larger. The combination shows mainly the features of $H_2O + O(^1D)$, with contributions of photolysis at altitudes above 50 km.
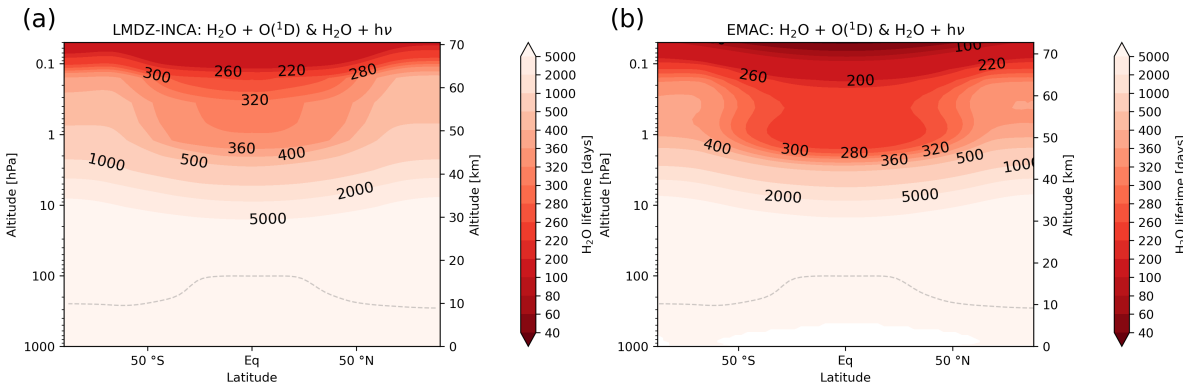
Figure 6. Zonal mean (photo-)chemical H_2O lifetime in days dependent on photolysis and reaction with $O(^1D)$ for LMDZ-INCA (a) and EMAC (b). Figure A5, showing both reactions independently, can be found in the appendix.

Clearly, the (photo-)chemical destruction increases with altitude. However, our results show that the perturbation doesn't decrease with altitude. To verify the chemical loss and production of water vapour we introduced an additional diagnosis within EMAC. It is a budget calculation for all chemical loss and production terms with respect to water vapour. Further information on our setup can be found in the supplementary files *meccanism.pdf* and *scavinism.pdf* and the general explanation in the supplement of Sander et al. (2005). We find that 29 % and 60 % of the annual emitted water vapour (Table 2) is destroyed for ZEHST and LAPCAT, respectively, which is generally in agreement with Fig. 6 that indicates larger (photo-)chemical H_2O losses at higher altitudes. The absolute values of H_2O loss are shown as dark blue bars in Fig. 7.

$$H_2O + h\nu \rightarrow H + OH \tag{2}$$

$$H_2O + O(^1D) \rightarrow 2\,OH \tag{3}$$

405 $$HO_2 + OH \rightarrow H_2O + O_2 \tag{4}$$

The main drivers are photolysis and the reaction with $O(^1D)$ (Eq. 2 and 3, Fig. 7 upper blue bars), where the reaction with $O(^1D)$ dominates for both aircraft scenarios. The other reactants responsible for H_2O destruction, N_2O_5, $ClNO_3$ and $BrNO_3$, are not significantly contributing.
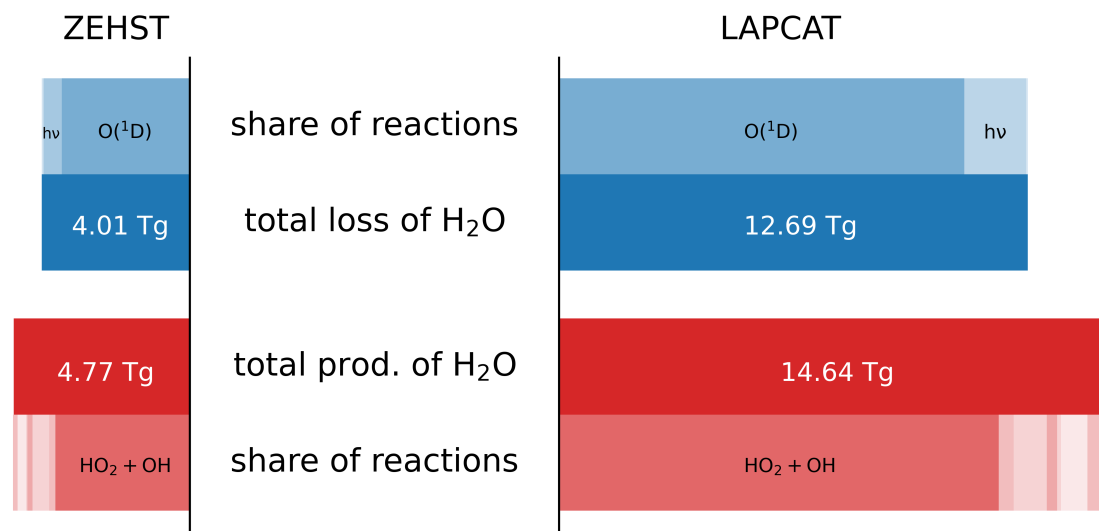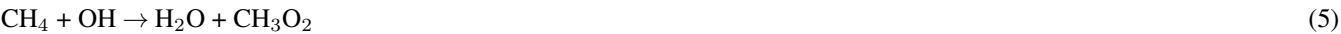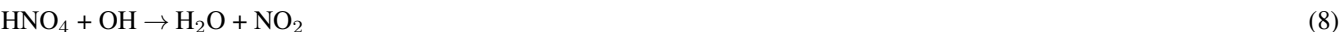

Figure 7. Bar plot of annual chemical loss and production perturbation of H_2O at stratospheric altitudes (100-0.1 hPa) for the ZEHST (left) and the LAPCAT (right) scenarios due to emitted trace gases (scenario-reference). This diagnosis includes a total of five H_2O destroying and 45 H_2O producing chemical reactions. The most relevant reactions of loss and production are shown as bright red and blue bars. Additionally, all dominant reactions of production are presented in detail in Fig. 8.

However, there is not only loss but also production of water vapour, which even overcompensates the loss by 0.76 Tg and 1.95 Tg in the case of ZEHST and LAPCAT, respectively (dark red bars). This equals an increase of the initial annual perturbation above 18 km by 5.53 % for the former and 9.32 % for the latter. The resulting change from emissions and (photo-)chemistry is balanced by transport to the troposphere. The most important reaction for water vapour production is Eq. 4, which on one hand destroys hydroxyl and hydroperoxyl and on the other hand produces water vapour.

$$CH_4 + OH \rightarrow H_2O + CH_3O_2 \tag{5}$$

415    $HCHO + OH \rightarrow CO + H_2O + HO_2$ (6)

$HNO_3 + OH \rightarrow H_2O + NO_3$ (7)

$HNO_4 + OH \rightarrow H_2O + NO_2$ (8)

We call the surplus of production over destruction net-recombination. This net-recombination originates from different sources and the significant reactions for production are shown in Fig. 8. Absolute values of production, 4.77 Tg/yr and 14.6
420   Tg/yr for ZEHST and LAPCAT, originally from Fig. 7 are shown here with additional information. In total, 45 reactions are contributing to H_2O production and we grouped the reactions in four different categories, which are reactions with C-, N-, Cl- and H-O-compounds. The main contributors by far is the HO_x-cycle (green) followed by either more efficient methane oxidation for LAPCAT (red) or contributions of nitric acids HNO_3 and HNO_4 for ZEHST (blue). The ratio of the categories is different for the two altitudes. H-O-compounds contribute more for emission at the higher altitude.
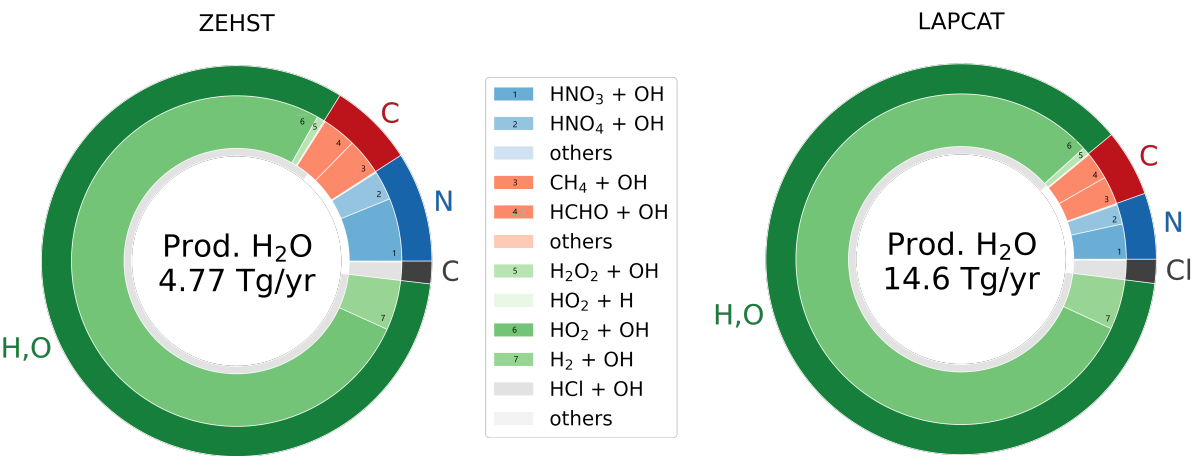
Figure 8. Pie plots on chemical reactions responsible for H_2O production derived from the EMAC simulation results (scenario-reference). Left: ZEHST scenario. Right: LAPCAT scenario. The darker outer ring shows the molecular category the reactions belong to (carbon-, nitrogen-, chlorine- or hydrogen-based). The total sum of H_2O production is written in the center. The colored inner ring shows the proportion of different reactions within each category. We added black numbers in the legend and the bright inner ring to represent the relation in addition to colours.

425   The photochemical depletion of H_2O and shift to H_2 concentrations (Brasseur and Solomon, 2005, e.g. Fig. 5.23, p. 312) is clearly not limiting the water vapour perturbation lifetime at these emission altitudes. So instead to the expected removal

of emitted H_2O by photochemical depletion, we found a before unknown importance of water vapour recombination for hypersonic emissions. Several reactions including the hydroxyl radical actually overcompensate the photochemical depletion of H_2O perturbations. The overcompensation results in a net-recombination (recombination-depletion > 0), that is driven by

430 HO_x recombination (mainly Eq. 4), an increased methane (Eqs. 5 and 6) and nitric acid oxidation (Eqs. 7 and 8). Both models show an increase in H_2O perturbation lifetime and H_2O perturbation at the higher altitude, which is further increased by the net-recombination. Our finding is robust with good agreement between the two models.

5.2 Nitrogen Oxides NO_x and Ozone O_3

Continuous emission of NO_x ($NO + NO_2$) of hypersonic aircraft has a significant impact on ozone chemistry. The family of perturbed NO-compounds is collectively described as NO_y (NO_x + and their nitrogen reservoir species). While NO_x is very reactive in catalytic cycles of ozone chemistry, NO_y additionally includes more stable molecules, like nitric acid (HNO_3), that act as a sink and remove NO-compounds from catalytic ozone cycles for a longer time compared to NO_x. Figure A4 shows the perturbation of NO_x for each model and each aircraft fleet. In general, the perturbation patterns are similar, but EMAC results show a more detailed perturbation pattern. For LMDZ-INCA we see a general NO_x increase, whereas in EMAC, additionally, a decrease is visible at approximately 1 hPa upwards ranging from equatorial regions to midlatitude regions for LAPCAT. In comparison, LMDZ-INCA shows one cluster of NO_x perturbation originating from the emission location (purple bar), while EMAC shows several (some not significant) clusters. The clusters locations seem to overlap, but the larger emission of LAPCAT makes it difficult to distinguish the clusters, as it covers the clusters interspace. The clusters appear at two levels, i.e. at cruise altitudes and at higher altitudes, just below 1 hPa. Results for the lower flying aircraft are more often outside of the 5 % uncertainty margin in comparison to the higher flying aircraft. This may be related to the larger emission of the latter, resulting in a larger perturbation which differs from zero perturbation with higher confidence.

As mentioned before, NO_x are very reactive in catalytic cycles of ozone chemistry. The perturbation of ozone resulting mainly from H_2O and NO_2 emission is shown in Fig. 9. The correlation between the increase of NO_x and the decrease of O_3 is clearly visible in the patterns at mid-stratospheric altitudes and especially at the cruise altitudes. LMDZ-INCA shows a slight increase originating from the tropical UTLS and a decrease with multiple clusters everywhere else, apart from no perturbation at lower latitudes at the highest altitude. EMAC results show a higher vertical resolution pattern with clusters of O_3 increase and decrease, which may be due to the higher vertical resolution of EMAC (90 vertical grid levels) compared to LMDZ-INCA (39 vertical grid levels) in this study. The O_3 increase in areas below an O_3 decrease has already been reported by Solomon et al. (1985) and they expect a larger effect for lower latitudes, which would agree with our results. Noteworthy is that the area of O_3 increase overlaps with the area where NO_x perturbations are close to zero. Additionally, more of the high-energy radiation should reach lower altitudes due to the decrease above the area of O_3 increase. To conclude, the uncertainties due to the annual variability are lower in LMDZ-INCA compared to EMAC for both O_3 and NO_x, highlighting the significance of LMDZ-INCA results. The larger vertical resolution in EMAC could explain the different uncertainty value ($p < 0.05$ for EMAC, $p < 0.001$ for LMDZ-INCA), since it allows more detailed perturbation patterns, which is not model-specific, but resolution-specific. If this is the case, this originates from the difference in vertical resolutions and not from the models themselves. The total reduction of O_3 is listed in Table 4. In general, results are of the same order of magnitude. Both models show the same trend that the higher flying aircraft fleet has a larger impact on O_3 and for both aircraft the perturbation is slightly larger in LMDZ-INCA results.
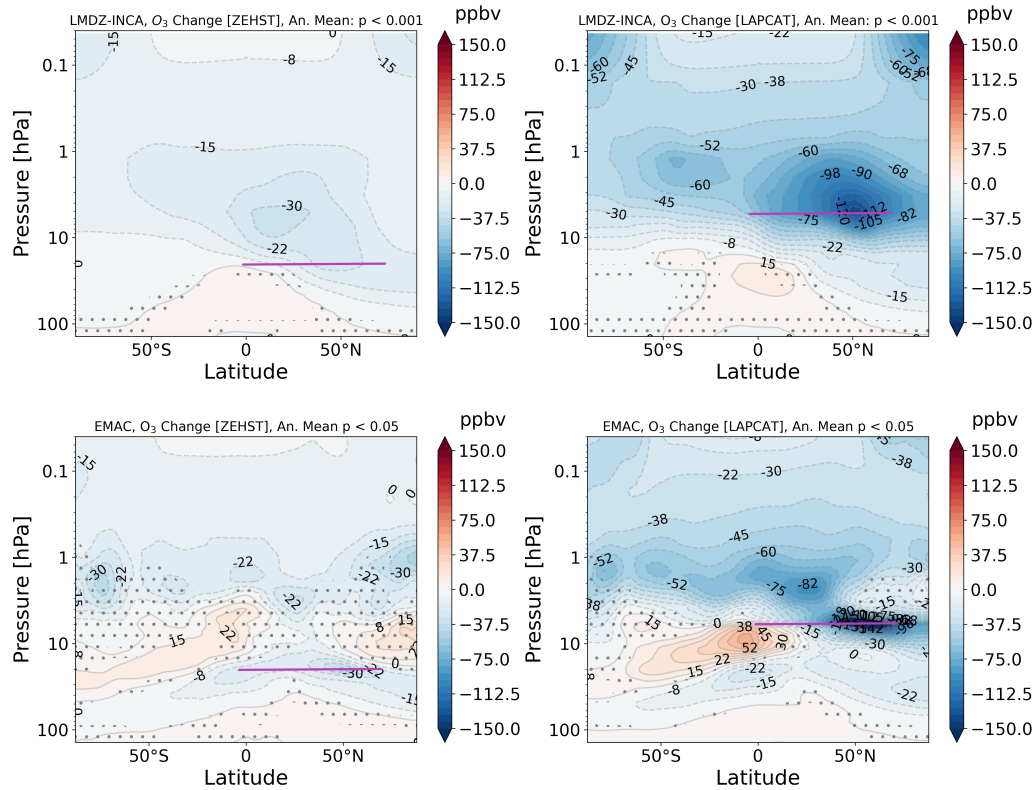
Figure 9. Multi-annual mean (2010-2014) of ozone perturbation (ppbv) for the ZEHST scenario (left) and the LAPCAT scenario (right) for both models LMDZ-INCA (top) and EMAC (bottom). Purple lines represent respective cruise altitudes. Hatched areas are characterized by a p-value higher than the threshold indicated in the title of each plot.

Table 4. Relative total ozone mass change for each model and each aircraft fleet.

Scenario	EMAC	LMDZ-INCA
ZEHST	-0.068 %	-0.097 %
LAPCAT	-0.14 %	-0.17 %

6 Radiation and Climate

465   The radiative forcing (RF) caused by atmospheric composition changes depends very much on location (Lacis et al., 1990; Riese et al., 2012). In our results, the largest water vapour concentration change appears at lower stratospheric altitudes and increases poleward (Fig. A2, Fig. A3). The differences between the ZEHST and LAPCAT scenario, except for magnitude, are

small. Additionally, we described the ozone increase in the lower tropical stratosphere, where the RF sensitivity and air density is larger (concentration changes not shown). Hence, according to Lacis et al. (1990); Riese et al. (2012) we expect a warming
470   for both ozone and water vapour changes.

    The annual radiative impact was calculated with the metric stratosphere adjusted radiative forcing at tropopause level using the equilibrium perturbation of H_2O, O_3 and CH_4. Atmospheric composition changes were used to calculate the RF with both models. The spin-up phase was three months and the averaged result is based on twelve monthly means. The resulting RF for both models and both aircraft fleets are listed in Table 5 with the LAPCAT scenario showing larger values mainly due to the
475   larger water vapour perturbation. The normalized RF per teragram of water vapour perturbation is in good agreement with an average and standard deviation of 0.43 ± 0.02 mW$(m^2*Tg)^{-1}$ and 0.39 ± 0.02 mW$(m^2*Tg)^{-1}$ for EMAC and LMDZ-INCA, respectively. Another measure, the RF per teragram of annual water vapour emission, shows that the normalized RF correlates with altitude and the values are 25-41 % larger for LAPCAT in both model results.

Table 5. Radiative forcing per year in mWm^{-2}, per teragram of H_2O perturbation and per teragram of annual water vapour emission (from Table 2), both in mW$(m^2Tg)^{-1}$, for each scenario and model calculated with atmospheric composition changes of H_2O, O_3 and CH_4.

Scenario	EMAC mWm^{-2}	LMDZ-INCA mWm^{-2}	EMAC mW$(m^2$ Tg$)^{-1}$	LMDZ-INCA mW$(m^2$ Tg$)^{-1}$	EMAC mW$(m^2$ Tg$)^{-1}$	LMDZ-INCA mW$(m^2$ Tg$)^{-1}$
ZEHST	20.95	15.42	0.44	0.40	1.52	1.12
LAPCAT	40.31	33.49	0.41	0.37	1.90	1.58

    The perturbations of H_2O, O_3 and CH_4 above the meteorological tropopause were used to calculate the RF (approximately
480   100 hPa at tropical and 300 hPa at polar latitudes). The direct impact of hydrogen perturbation on RF is not significant and their indirect effect, i.e. on O_3 and H_2O mixing ratios is included and will be reported in a separate publication in more detail (Pletzer and Grewe, 2022, in prep). In comparison, the contribution to RF of H_2O is largest, followed by O_3 and a negative RF due to CH_4 reduction. The negative RF of the latter is due to the enhanced methane oxidation and is larger for the LAPCAT scenario where hydroxyl radicals are clearly more active (Fig. 7). The detailed values with short- and longwave contributions
485   are listed in Table 6.

    LMDZ-INCA shows a smaller longwave RF (LW RF) and a larger negative shortwave RF (SW RF) for H_2O compared to EMAC. Ozone longwave RF has a negative sign for EMAC and positive for LMDZ-INCA. The differences in magnitude and sign of O_3 longwave RF may originate from the varying atmospheric composition changes in EMAC with areas of ozone increase and decrease. This altitude dependency very much affects the contribution to RF as has been shown by Lacis et al.
490   (1990) and Hansen et al. (1997). An additional test shows that the ozone increase in the UTLS compensates the negative longwave forcing due to the high sensitivity to ozone changes and explains the positive longwave value for LMDZ-INCA. Ozone shortwave RF is generally larger by 40-44 % for LMDZ-INCA compared to EMAC. Methane net RF is 1-2 order of magnitude smaller for EMAC compared to LMDZ-INCA. A comparison of change in global methane lifetimes is shown in

Table 6. Short- and longwave contributions (respectively SW and LW) to radiative forcing (RF) in $\mathrm{mWm^{-2}}$.

Aircraft	Model	Perturbation	SW RF	LW RF	RF
ZEHST	LMDZ-INCA	O_3	3.43	0.35	3.78
	EMAC	O_3	2.38	-0.73	1.65
	LMDZ-INCA	CH_4	-	-	-1.38
	EMAC	CH_4	-	-	-0.015
	LMDZ-INCA	H_2O	-2.27	15.29	13.02
	EMAC	H_2O	-1.59	20.90	19.32
LAPCAT	LMDZ-INCA	O_3	5.72	1.84	7.56
	EMAC	O_3	4.11	-0.78	3.34
	LMDZ-INCA	CH_4	-	-	-2.47
	EMAC	CH_4	-	-	-0.046
	LMDZ-INCA	H_2O	-4.25	32.65	28.40
	EMAC	H_2O	-2.27	39.90	37.01

the appendix. There, methane lifetime change is larger for the LAPCAT compared to the ZEHST scenario for both models and the methane lifetime is in general less for EMAC compared to LMDZ-INCA for both ZEHST and LAPCAT scenarios by a factor of three and two, respectively. To conclude, the reason for the different magnitude in methane net RF is not fully clear and should originate from the RF calculation. However, the contribution of methane to RF is small in both models compared to H_2O and O_3 and should not affect our results.

For the largest contribution to RF, the H_2O perturbation, we have performed a comparison to other radiation calculations. The performance test was done like in Myhre et al. (2009). That means we calculated the impact on RF by an increase of water vapour mixing ratio from 3.0 to 3.7 ppmv above the tropopause. The LMDZ-INCA result is 0.18 $\mathrm{Wm^{-2}}$, which is below the mean of Myhre et al. (mean 0.25 $\mathrm{Wm^{-2}}$, range $0.16 - 0.38$ $\mathrm{Wm^{-2}}$), while the EMAC result is larger than the mean with 0.28 $\mathrm{Wm^{-2}}$. Both models are in the range of different models presented by Myhre et al., with LMDZ-INCA at the lower and EMAC in the mid-upper range.

Perturbations at tropospheric altitudes were neglected mainly due to the large variability of water vapour, either with a reset to reference water vapour during the perturbation simulations (LMDZ-INCA) or due to exclusion in the RF calculations (EMAC). Hence, for EMAC the H_2O perturbations at tropospheric altitudes are not zero and therefore will contribute to the RF calculations. However, the upper tropospheric water vapour perturbations have a very large variability, since the 5 % confidence intervals for the mean are ±106 % and ±33 % for the ZEHST and LAPCAT scenarios, respectively. In comparison, for H_2O perturbations above the tropopause, variability is significantly smaller with ±3.1 % and ±1.8 % for the ZEHST and LAPCAT scenarios, respectively. Hence, water vapour perturbation in the upper troposphere could significantly contribute to RF, but the

associated error due to the large variability is significantly larger. Nonetheless, we calculated the RF with EMAC including the tropospheric perturbations for comparison (see Table A1). We found that the RF increases by approximately 51 to 63 % when the upper tropospheric perturbations are included.

7 Discussion

7.1 Limitations of the Model Simulations

7.1.1 Aerosol and Water Vapour from Volcanic Origin

In our model simulations, we assume an atmosphere without volcanic eruptions. However, volcanic eruptions could occur during the decades of operation of new aircraft. Volcanic emissions, like water vapour or sulphate aerosols, affect the atmospheric composition in the stratosphere, especially through heterogeneous chemistry, and these changes are strongly dependent on latitude and season. The changes of lower stratospheric water vapour changes due to volcanic eruptions is on the order of two years and affect ozone concentrations (Stenke and Grewe, 2005). Sulfate aerosols are known to increase temperatures in the tropics and could in turn enhance the Brewer-Dobson circulation, eventually slightly reducing the climate impact of hypersonic transport. Overall, the topic is very complex in itself and how hypersonic emissions and volcanic emissions influence each other remains to be answered with robust and topic specific simulations.

7.1.2 Strengthening of the Brewer-Dobson Circulation

In our model simulations we use atmospheric composition projections for the years 2050-2064 combined with present day meteorology (2000-2014). Hence, projections of the dynamic component are not included in our simulations. The main reason is, that reanalysis data from the future is simply not available for nudging. Using another method was not an option, since we rely on nudging to have the same meteorology in both models for a high signal-to-noise ratio. However, the changes of dynamic processes like the Brewer-Dobson circulation due to climate change are very likely significant and we therefore discuss the topic briefly (Butchart et al., 2006; Shepherd and McLandress, 2011). The associated transport is the dominant factor of water vapour perturbation lifetime and therefore of the climate impact of hypersonic aircraft. An increase in strength of the stratospheric and mesospheric circulation would most likely reduce the climate impact of hypersonic aircraft. Butchart et al. (2006) estimate the troposphere-stratosphere mean mass exchange rate to increase with 2 % per decade (with considerable differences between the models). That would result in an approximately 8-10 % stronger circulation from 2050-2064 and in turn – if the effect can really be directly translated to perturbation lifetime – the climate impact of hypersonic aircraft would be reduced by approximately the same percentage.

7.2 Atmospheric Composition Changes

Here, we focus on the comparison to the publication by Kinnison et al. (2020). They estimate the ozone, water vapour, NO_x and HO_x perturbations by a fleet of hypersonic aircraft in independent scenarios where aircraft, powered with conventional fuel, fly

at 30 km and 40 km, using the coupled chemistry-climate model WACCM (Whole Atmosphere Community Climate Model). Similar to our model setups, WACCM simulates atmospheric chemistry and dynamics. For more detailed information, please refer to their publication. Similar to our setup they look at atmospheric conditions for the year 2050, however the averaged
545   annual results are based on one year, while ours represent the mean over five years. In turn, a larger deviation from the long-term mean could be expected for their results. The total annual emission in their setup amounts to 58.3 Tg of H_2O and 0.94 Tg of NO_2, which is approximately three to four times larger for the former, and 30 to 47 times larger for the latter, compared to the annual values of the HIKARI data.

In agreement with our result, the H_2O perturbation for the higher flying aircraft fleet is significantly larger and the perturba-
550   tion patterns agree very well with the maximum perturbation being at midlatitudes at the northern hemisphere and at the cruise altitude. In their case the total emission per trace gas is the same for both altitudes, which is not the case in our study, since the emissions in HIKARI are based on two different aircraft designs. Total values of mass perturbation were not published for H_2O and thus cannot be compared with ours. We presented the (photo-)chemical lifetime in Fig. 6. Here, the agreement of latitudinal and altitude features with Kinnison et al. (2020, Fig. 3) is very good in general. There are differences in magnitude
555   from 50 km upward, increasing with altitude where photolysis is dominant. If this originates from WACCM covering more of the atmosphere compared to our models, and thus being more accurate at 50 km upwards, is an open question. However, the stratosphere is well represented in the models used here, which is most important for the topic of our study, and the equilibrium mass perturbation at mesospheric altitudes is insignificant in comparison to stratospheric altitudes.
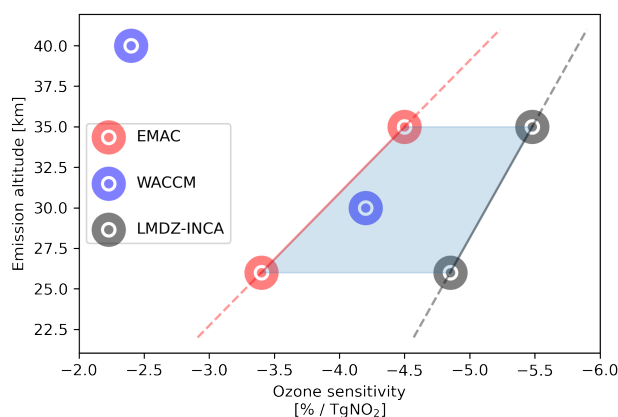
Figure 10. Ozone sensitivity from three different models WACCM, EMAC and LMDZ-INCA dependent on altitude. Results from this work were calculated using values from Table 2 and Table 4. Results for WACCM were published by Kinnison et al. (2020, Table 2). The shaded area highlights the good agreement of LMDZ-INCA and EMAC results with WACCM results for the region from approximately 26-35 km altitude.

7.2.1 Ozone Sensitivity

560 The calculated ozone sensitivity with -4.2 % / Tg NO_2 and -2.4 % / Tg NO_2 for 30 km and 40 km altitude (Kinnison et al., 2020, Table 2) is of the same order of magnitude compared to our results with -3.4 % / Tg NO_2 and -4.5 % / Tg NO_2 for EMAC and -4.9 % / Tg NO_2 and -5.5 % / Tg NO_2 for LMDZ-INCA at 26 km and 35 km altitude, respectively. Figure 10 shows both results from our study and their study. Our results have a positive correlation between ozone sensitivity and altitude. This might point to a maximum of absolute ozone sensitivity at around 35 km altitude, since the absolute value for WACCM

565 at 40 km altitude is already much smaller and the models seem to agree very well for the region between 26 and 35 km. The assumed tropical maximum of ozone mixing ratio of 31 km overlaps with this region and is very close to the maximum value. However, the altitude of emission often does differ from perturbation maxima of NO_x and O_3. Be aware that we are only presenting two data points per model and to come to conclusions regarding the largest value of ozone sensitivity might be inaccurate. Additionally, there are some differences between the setups, e.g. Kinnison et al. estimate ozone sensitivity based on

570 NO_x perturbations only and with a larger amount, while we do look at the combined effects by NO_x, H_2O and H_2 emission. Furthermore, the HIKARI data includes a vertical distribution of emission, in which take off and landing are present, and the fleet comprises not only hypersonic but subsonic aircraft as well, while they inject the emission in a single layer. The effect of tropospheric water vapour emission on SWV is negligible due to the tropical tropopause coldpoint, but NO_x emitted in the tropical troposphere may be transported to stratospheric altitudes and increase the uncertainty of the comparison. Note that in

575 another set of EMAC simulations, from a forthcoming publication (Pletzer and Grewe, 2022, in prep), where NO_x is emitted in a single layer, we see an approximately equal ozone sensitivity at 30 km and 38 km for tropical and midlatitudinal regions, while for northern polar regions the lower altitude has a sensitivity nearly twice as much as the higher altitude and shows a negative correlation very similar to Kinnison et al. (2020).

7.2.2 Contrail Formation

580 Another type of atmospheric composition change that affects climate is the formation of contrails. A study from Stenke et al (2008) estimates the change in contrail formation and the change of contrail radiative forcing for subsonic and supersonic aircraft, by replacing parts of the subsonic fleet with supersonic aircraft. According to the authors the change in contrail radiative forcing and change in total contrail cover is very small. However, they report a shift of contrail cover from mid latitudes (200 hPa) to low latitudes (supersonic cruise altitude). For hypersonic aircraft this relation might be changed. Hypersonic

585 aircraft are flying above the tropical tropopause, where temperatures are warmer, and hence do not form contrails in the tropics. Therefore, the replacement of subsonic with hypersonic aircraft would probably lead to a reduction of contrail radiative forcing.

7.3 Comparison to Emissions at Lower Altitudes

Zhang et al. (2021, Figure 11) published an altitude dependent comparison of ozone and water vapour RF normalized to fuel use. To compare their results on climate impact we used their emission index (EI(H_2O) = 1,237 g(H_2O)/kg fuel) and fuel use

590 (47.18 Tg) to recalculate their results to RF per emitted water vapour in teragram. With the above values, we extracted the

linear relation of $0.1 \,\mathrm{mW\,m^{-2}}/2\mathrm{km}$ for an increase of RF with altitude. The extrapolation to ZEHST and LAPCAT cruise altitudes resulted in $0.93 \,\mathrm{mW\,m^{-2}}$ and $1.56 \,\mathrm{mW\,m^{-2}}$ for ZEHST and LAPCAT, respectively. Compared to our results (1.1-1.5 $\mathrm{mW\,m^{-2}}$ and 1.6-$1.9 \,\mathrm{mW\,m^{-2}}$ for ZEHST and LAPCAT, respectively), presented in Table 5, the here calculated values are generally lower than the EMAC results, especially compared to ZEHST. LMDZ-INCA results are lower for ZEHST compared to the extrapolation, however agree astonishingly well for LAPCAT. Clearly, the linear relation is not a perfect fit, however it shows the same trend and the order of magnitude agrees very well.

7.4 Comparison to the Climate Impact of Other Aircraft Designs

For a better comparison of hypersonic to sub- and supersonic aircraft we included Fig. 11. It shows an enhancement factor, i.e. the ratio of the climate impact of a specific aircraft compared to a conventional subsonic aircraft and hence without unit, depending on altitude. The numbers shown there were calculated using the climate response model AirClim (Grewe and Stenke, 2008; Dahlmann et al., 2016). The subsonic estimate is based on contrail formation, CO_2, H_2O and NO_x (short-lived ozone, primary mode ozone, methane) effects. The comparison is based on results from this study and Grewe et al. (2007, 2010); Grewe (2021). While subsonic is the reference case with a value of 1, supersonic aircraft show a climate impact that is increasing with altitude. The hypersonic aircraft ZEHST follows that trend with an enhancement factor of approximately 20 (near-surface temperature change or RF normalized to revenue passenger kilometers). However, the enhancement factor of the second hypersonic aircraft LAPCAT (PREPHA) is less than 10 due to its higher passenger capacity. Hence, a larger aircraft size, i.e. larger passenger number, is clearly a promising design option to reduce the climate impact per passenger and can compensate the climate impact due to higher cruise altitudes. The error estimate (blue shaded area) includes the tropospheric region with its very large variability (see page 29). Blue squares represent an aircraft of type LAPCAT MR3, developed in the STRATOFLY project, for four different altitudes and based on a single trajectory (Viola et al., 2021a, b). There, the increasing climate impact with altitude is clearly visible.

7.5 Climate Impact of Hypersonic Aircraft

Estimates on the climate impact of hypersonic aircraft barely exist. A recent estimate was published by Ingenito (2018). He approximates the climate impact by a fleet of hypersonic aircraft (type LAPCAT II MR2.4, 2015) based on water vapour perturbation only. In his study a fleet of 200 hypersonic aircraft fly from Brussels to Sydney 365 days a year and emit $376 \,\mathrm{Tg}$ of water vapour, which results in a water vapour perturbation that increases surface temperature by $100 \,\mathrm{mK}$. We want to mention that the estimate is based on a correlation of an increase in global atmospheric water vapour and near-surface temperature from a third publication and the whole calculation can be described as a 1D box model. For comparison to our results in Fig. 11, we normalize the change in surface temperature with passenger kilometers (pax-km). Therefore, we assume a distance of 16,367 km between Brussels and Sydney and a passenger capacity of 300 (LAPCAT II) and obtain a normalized near-surface temperature change of $396 \ 10^{-12} \,\mathrm{mK(pax-km)^{-1}}$. This equals an enhancement factor of 61 and hence their estimate of the climate impact of hypersonic aircraft is 61 as much as subsonic aircraft. Compared to the enhancement factors in Fig. 11, this value is outside of the uncertainty range of our study. The upper limit of the uncertainty range is equal to RF calculations
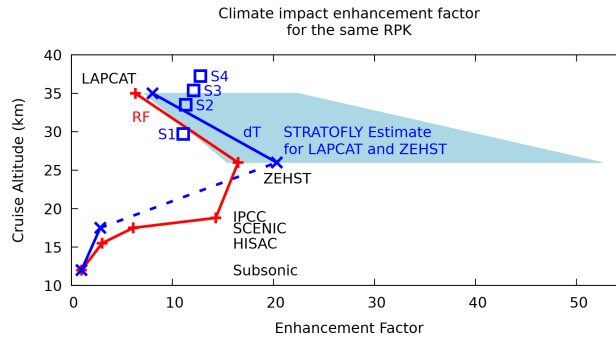
Figure 11. Radiative forcing (red) 50 years after entry into service (EIS) of a fleet of the respective aircraft and the near-surface temperature change (blue) based on the HIKARI project results. RPK (unit pax-km) refers to the revenue passenger kilometers, i.e. total kilometers travelled by all passengers on an aircraft or on a fleet of aircraft. The shaded area shows an uncertainty range from this work. This figure is taken from Grewe (2021) and includes the values of four STRATOFLY MR3 versions for different altitudes (S1 to S4) based on data published by Viola et al. (2021a, Table 2).

with composition changes including upper tropospheric water vapour. These were neglected in the main calculations due to the large variability and the focus on stratospheric perturbation of trace gases.

We mentioned the significant contribution of upper tropospheric water vapour to RF in our model simulations with EMAC and want to elaborate some more, as this is important for comparison. In general, the lifetime of water vapour is comparably short at tropospheric altitudes (spreading from hours to approximately six months, Fig. 6a in Grewe and Stenke (2008)). However, in our study the main emission is at midlatitudes, where water vapour lifetime is between 7 days and one month according to the reference. We did not test how well the tropospheric perturbation is represented in our model, since we focused on stratospheric perturbations in the EMAC setup. In EMAC simulations, the tropospheric water vapour was not reset nor nudged to ECMWF data, in contrast to the LMDZ-INCA simulations. Therefore, the variability introduces a large error range in the upper tropospheric water vapour results compared to the results for the stratosphere in EMAC.

8 Summary

In this study we calculated the radiative forcing and the climate impact of two different hypersonic aircraft designs, both fueled with liquid hydrogen. The difference in cruise altitude (26 km and 35 km) results in significant differences in atmospheric perturbations, perturbation lifetime and in turn climate impact. Clearly, water vapour is the largest contributor for the latter. We find an efficient (photo-)chemical destruction of H_2O at higher altitudes, as expected based on theory (Brasseur and Solomon, 2005, e.g. Fig. 5.23, p. 312). But we did not see a smaller H_2O perturbation at the higher emission altitude, which agrees with the tendency in the study by Kinnison et al. (2020). Our analysis shows for the first time that the recombination to H_2O overcompensates the (photo-)chemical destruction of emitted H_2O, which results in a longer H_2O perturbation lifetime at the higher altitude (35 km). The overcompensation originates from an increased CH4 and HNO3 oxidation in addition to the HO_x

recombination. This trend may change at even higher altitudes, where water vapour lifetime decreases and, more importantly, the lifetime of HO_x and H_2 increases substantially. Whether the recombination of emitted water vapour is affected has not been

645   tested at these altitudes. The finding of longer H_2O perturbation lifetime and recombination contributes to the understanding of chemistry at stratospheric and lower mesospheric altitudes. For ozone, we report an overall depletion of the ozone layer, with a decrease at middle-to-upper stratospheric altitudes and an increase at lower stratospheric altitudes. This results in radiative warming for both aircraft, with a larger effect for the higher flying aircraft. The radiative impact of increased hydrogen is not significant compared to the other contributors and has a comparably small indirect effect by contributing to atmospheric

650   perturbations of CH_4, H_2O and O_3. This will be addressed in more detail in a follow-up publication. The results can be deemed robust due to the usage of two high-end chemistry climate models and the performance validation of radiative forcing due to stratospheric water vapour perturbation. To conclude briefly, the impact on climate of aircraft emitting water vapour and flying above the tropopause increases very much with altitude, since water vapour radiative forcing is significantly larger than ozone radiative forcing, which has a more complex altitude dependency. This is clearly shown by the increase of water vapour

655   perturbation lifetime and normalized radiative forcing with altitude. Due to larger fuel consumption with higher speed at high cruise altitudes on one hand, and the atmospheric conditions at these cruise altitudes (recombination, lifetime of H_2O) on the other hand, hypersonic aircraft have a considerable larger climate impact than subsonic and supersonic aircraft.

31

References

Archer, D. and Brovkin, V.: The millennial atmospheric lifetime of anthropogenic CO2, Climatic Change, 90, 283–297, https://doi.org/10.1007/s10584-008-9413-1, https://doi.org/10.1007/s10584-008-9413-1, 2008.

Archer, D., Eby, M., Brovkin, V., Ridgwell, A., Cao, L., Mikolajewicz, U., Caldeira, K., Matsumoto, K., Munhoven, G., Montenegro, A., and Tokos, K.: Atmospheric Lifetime of Fossil Fuel Carbon Dioxide, Annual Review of Earth and Planetary Sciences, 37, 117–134, https://doi.org/10.1146/annurev.earth.031208.100206, https://doi.org/10.1146/annurev.earth.031208.100206, 2009.

Blanvillain, E. and Gallic, G.: HIKARI: Paving the way towards High Speed Air Transport, 20th AIAA International Space Planes and Hypersonic Systems and Technologies Conference, https://doi.org/10.2514/6.2015-3676, https://arc.aiaa.org/doi/abs/10.2514/6.2015-3676, 2015.

Brasseur, G. and Solomon, S.: Aeronomy of the middle atmosphere: chemistry and physics of the stratosphere and mesosphere, no. v. 32 in Atmospheric and oceanographic sciences library, Springer, Dordrecht ; [Great Britain], 3rd rev. and enlarged ed edn., oCLC: ocm62343740, 2005.

Bundke, U., Smit, H., Sauvage, B., Gerbig, C., Hermann, M., Berkes, F., Nédélec, P., Gallagher, M., Ziereis, H., Boulanger, D., Thouret, V., and Petzold, A.: IAGOS time series, AERIS [data set], https://doi.org/10.25326/06, last access: 2022-04-06, 2018.

Butchart, N., Scaife, A. A., Bourqui, M., de Grandpré, J., Hare, S. H. E., Kettleborough, J., Langematz, U., Manzini, E., Sassi, F., Shibata, K., Shindell, D., and Sigmond, M.: Simulations of anthropogenic change in the strength of the Brewer–Dobson circulation, Climate Dynamics, 27, 727–741, https://doi.org/10.1007/s00382-006-0162-4, https://doi.org/10.1007/s00382-006-0162-4, 2006.

Cohen, Y., Marécal, V., Josse, B., and Thouret, V.: Interpol-IAGOS: a new method for assessing long-term chemistry–climate simulations in the UTLS based on IAGOS data, and its application to the MOCAGE CCMI REF-C1SD simulation, Geosci. Model Dev., 14, 2659–2689, https://doi.org/10.5194/gmd-14-2659-2021, 2021a.

Cohen, Y., Thouret, V., Marécal, V., and Josse, B.: Interpol-IAGOS software, https://doi.org/10.25326/81, last access: 2022-04-06, 2021b.

CORDIS: EU research results: HIKARI, https://cordis.europa.eu/project/id/313987, [Online; accessed 4-May-2022], 2015.

Crutzen, P. J.: The influence of nitrogen oxides on the atmospheric ozone content, Quarterly Journal of the Royal Meteorological Society, 96, 320–325, https://doi.org/10.1002/qj.49709640815, http://onlinelibrary.wiley.com/doi/abs/10.1002/qj.49709640815, _eprint: https://rmets.onlinelibrary.wiley.com/doi/pdf/10.1002/qj.49709640815, 1970.

Crutzen, P. J.: SST's: A Threat to the Earth's Ozone Shield, Ambio, 1, 41–51, http://www.jstor.org/stable/4311946, publisher: [Springer, Royal Swedish Academy of Sciences], 1972.

Dahlmann, K., Grewe, V., Frömming, C., and Burkhardt, U.: Can we reliably assess climate mitigation options for air traffic scenarios despite large uncertainties in atmospheric processes?, Transportation Research Part D: Transport and Environment, 46, 40–55, https://doi.org/10.1016/j.trd.2016.03.006, https://www.sciencedirect.com/science/article/pii/S1361920916000353, 2016.

Dee, D. P., Uppala, S. M., Simmons, A. J., Berrisford, P., Poli, P., Kobayashi, S., Andrae, U., Balmaseda, M. A., Balsamo, G., Bauer, P., Bechtold, P., Beljaars, A. C. M., van de Berg, L., Bidlot, J., Bormann, N., Delsol, C., Dragani, R., Fuentes, M., Geer, A. J., Haimberger, L., Healy, S. B., Hersbach, H., Hólm, E. V., Isaksen, L., Kållberg, P., Köhler, M., Matricardi, M., McNally, A. P., Monge-Sanz, B. M., Morcrette, J.-J., Park, B.-K., Peubey, C., de Rosnay, P., Tavolato, C., Thépaut, J.-N., and Vitart, F.: The ERA-Interim reanalysis: configuration and performance of the data assimilation system, Quarterly Journal of the Royal Meteorological Society, 137, 553–597, https://doi.org/10.1002/qj.828, http://onlinelibrary.wiley.com/doi/abs/10.1002/qj.828, _eprint: https://rmets.onlinelibrary.wiley.com/doi/pdf/10.1002/qj.828, 2011.

695 Defoort, S., Serre, L., Grenon, R., Varnier, J., Carrier, G., Scherrer, D., and Narmada: ZEHST: environmental challenges for hypersonic passenger transport, 18th AIAA/3AF International Space Planes and Hypersonic Systems and Technologies Conference, https://doi.org/10.2514/6.2012-5873, https://arc.aiaa.org/doi/abs/10.2514/6.2012-5873, 2012.

Ehhalt, D. H. and Rohrer, F.: The tropospheric cycle of H_2: a critical review, Tellus B: Chemical and Physical Meteorology, 61, 500–535, https://doi.org/10.1111/j.1600-0889.2009.00416.x, https://doi.org/10.1111/j.1600-0889.2009.00416.x, 2009.

700 Eichinger, R. and Jöckel, P.: The generic MESSy submodel TENDENCY (v1.0) for process-based analyses in Earth system models, Geoscientific Model Development, 7, 1573–1582, https://doi.org/10.5194/gmd-7-1573-2014, https://gmd.copernicus.org/articles/7/1573/2014/, 2014.

Eichinger, R., Jöckel, P., Brinkop, S., Werner, M., and Lossow, S.: Simulation of the isotopic composition of stratospheric water vapour – Part 1: Description and evaluation of the EMAC model, Atmospheric Chemistry and Physics, 15, 5537–5555, https://doi.org/10.5194/acp-15-5537-2015, https://acp.copernicus.org/articles/15/5537/2015/, 2015a.

Eichinger, R., Jöckel, P., and Lossow, S.: Simulation of the isotopic composition of stratospheric water vapour – Part 2: Investigation of HDO / H_2O variations, Atmospheric Chemistry and Physics, 15, 7003–7015, https://doi.org/10.5194/acp-15-7003-2015, https://acp.copernicus.org/articles/15/7003/2015/, 2015b.

ESA: LAPCAT II, https://www.esa.int/Enabling_Support/Space_Engineering_Technology/LAPCAT_II, [Online; accessed 4-May-2022], 710 2015.

Falempin, F., Scherrer, D., Laruelle, G., Rostand, P., Fratacci, G., and Schultz, J.: French Hypersonic Propulsion Program PREPHA - Results, lessons and perspectives, in: 8th AIAA International Space Planes and Hypersonic Systems and Technologies Conference, American Institute of Aeronautics and Astronautics, Norfolk,VA,U.S.A., https://doi.org/10.2514/6.1998-1565, https://arc.aiaa.org/doi/10.2514/6.1998-1565, 1998.

715 Frank, F., Jöckel, P., Gromov, S., and Dameris, M.: Investigating the yield of H_2O and H_2 from methane oxidation in the stratosphere, Atmospheric Chemistry and Physics, 18, 9955–9973, https://doi.org/10.5194/acp-18-9955-2018, https://acp.copernicus.org/articles/18/9955/2018/, 2018.

Fuel Cells and Hydrogen: Joint Undertaking: Hydrogen-powered Aviation, https://www.fch.europa.eu/publications/hydrogen-powered-aviation, [Online; accessed 4-May-2022], 2020.

720 Gauss, M., Isaksen, I. S. A., Wong, S., and Wang, W.-C.: Impact of H_2O emissions from cryoplanes and kerosene aircraft on the atmosphere, Journal of Geophysical Research: Atmospheres, 108, https://doi.org/https://doi.org/10.1029/2002JD002623, https://agupubs.onlinelibrary.wiley.com/doi/abs/10.1029/2002JD002623, 2003.

Grewe, V.: Climate Impact of Hypersonic Aviation, State-of-the-Art Hypersonic Civilian Transportation: Design, Technologies and Environmental Impact, access via ls@vki.ac.be or secretariat@vki.ac.be, 2021.

725 Grewe, V. and Stenke, A.: AirClim: an efficient tool for climate evaluation of aircraft technology, Atmospheric Chemistry and Physics, 8, 4621–4639, https://doi.org/10.5194/acp-8-4621-2008, https://acp.copernicus.org/articles/8/4621/2008/, 2008.

Grewe, V., Brunner, D., Dameris, M., Grenfell, J., Hein, R., Shindell, D., and Staehelin, J.: Origin and variability of upper tropospheric nitrogen oxides and ozone at northern mid-latitudes, Atmospheric Environment, 35, 3421–3433, https://doi.org/https://doi.org/10.1016/S1352-2310(01)00134-0, https://www.sciencedirect.com/science/article/pii/S1352231001001340, 2001.

730 Grewe, V., Stenke, A., Ponater, M., Sausen, R., Pitari, G., Iachetti, D., Rogers, H., Dessens, O., Pyle, J., Isaksen, I. S. A., Gulstad, L., Søvde, O. A., Marizy, C., and Pascuillo, E.: Climate impact of supersonic air traffic: an approach to optimize a potential future supersonic

33

fleet; results from the EU-project SCENIC, Atmospheric Chemistry and Physics, 7, 5129–5145, https://doi.org/10.5194/acp-7-5129-2007, https://acp.copernicus.org/articles/7/5129/2007/, 2007.

Grewe, V., Plohr, M., Cerino, G., Muzio, M. D., Deremaux, Y., Galerneau, M., de Staint Martin, P., Chaika, T., Hasselrot, A., Tengzelius, U., and Korovkin, V. D.: Estimates of the climate impact of future small-scale supersonic transport aircraft – results from the HISAC EU-project, The Aeronautical Journal, 114, 199–206, https://elib.dlr.de/82770/, 2010.

Grewe, V., Bock, L., Burkhardt, U., Dahlmann, K., Gierens, K., Hüttenhofer, L., Unterstrasser, S., Rao, A. G., Bhat, A., Yin, F., Reichel, T. G., Paschereit, O., and Levy, Y.: Assessing the climate impact of the AHEAD multi-fuel blended wing body, Meteorologische Zeitschrift, 26, 711–725, https://doi.org/10.1127/metz/2016/0758, http://dx.doi.org/10.1127/metz/2016/0758, 2017.

Grewe, V., Gangoli Rao, A., Grönstedt, T., Xisto, C., Linke, F., Melkert, J., Middel, J., Ohlenforst, B., Blakey, S., Christie, S., Matthes, S., and Dahlmann, K.: Evaluating the climate impact of aviation emission scenarios towards the Paris agreement including COVID-19 effects, Nature Communications, 12, 3841, https://doi.org/10.1038/s41467-021-24091-y, https://www.nature.com/articles/s41467-021-24091-y, 2021.

Hansen, J., Sato, M., and Ruedy, R.: Radiative forcing and climate response, Journal of Geophysical Research: Atmospheres, 102, 6831–6864, https://doi.org/10.1029/96JD03436, http://doi.wiley.com/10.1029/96JD03436, 1997.

Helten, M., Smit, H. G. J., Sträter, W., Kley, D., Nédélec, P., Zöger, M., and Busen, R.: Calibration and performance of automatic compact instrumentation for the measurement of relative humidity from passenger aircraft, J. Geophys. Res.-Atmos., 103, 25 643–25 652, https://doi.org/10.1029/98JD00536, 1998.

Hoyer, S. and Joseph, H.: xarray: N-D labeled Arrays and Datasets in Python, Journal of Open Research Software, 5, https://doi.org/10.5334/jors.148, 2017.

Ingenito, A.: Impact of hydrogen fueled hypersonic airliners on the O_3 layer depletion, International Journal of Hydrogen Energy, 43, 22 694–22 704, https://doi.org/https://doi.org/10.1016/j.ijhydene.2018.09.208, https://www.sciencedirect.com/science/article/pii/S0360319918331379, 2018.

IPCC: Special Report on Aviation and the Global Atmosphere. Prepared in collaboration with the Scientific Assessment Panel to the Montreal Protocol on Substances that Deplete the Ozone Layer, in: Intergovernmental Panel on Climate Change, edited by Penner, J. E., Lister, D. H., Griggs, D. J., Dokken, D. J., and McFarland, M., pp. 1–373, Through Cambridge University Press, The Edinburgh Building Shaftesbury Road, Cambridge CB2 2RU England, 1999.

Jöckel, P., Sander, R., Kerkweg, A., Tost, H., and Lelieveld, J.: Technical Note: The Modular Earth Submodel System (MESSy) - a new approach towards Earth System Modeling, Atmospheric Chemistry and Physics, 5, 433–444, https://doi.org/10.5194/acp-5-433-2005, https://acp.copernicus.org/articles/5/433/2005/, 2005.

Jöckel, P., Tost, H., Pozzer, A., Brühl, C., Buchholz, J., Ganzeveld, L., Hoor, P., Kerkweg, A., Lawrence, M. G., Sander, R., Steil, B., Stiller, G., Tanarhte, M., Taraborrelli, D., van Aardenne, J., and Lelieveld, J.: The atmospheric chemistry general circulation model ECHAM5/MESSy1: consistent simulation of ozone from the surface to the mesosphere, Atmospheric Chemistry and Physics, 6, 5067–5104, https://doi.org/10.5194/acp-6-5067-2006, https://acp.copernicus.org/articles/6/5067/2006/, 2006.

Jöckel, P., Kerkweg, A., Pozzer, A., Sander, R., Tost, H., Riede, H., Baumgaertner, A., Gromov, S., and Kern, B.: Development cycle 2 of the Modular Earth Submodel System (MESSy2), Geoscientific Model Development, 3, 717–752, https://doi.org/10.5194/gmd-3-717-2010, https://gmd.copernicus.org/articles/3/717/2010/, 2010.

Jöckel, P., Tost, H., Pozzer, A., Kunze, M., Kirner, O., Brenninkmeijer, C. A. M., Brinkop, S., Cai, D. S., Dyroff, C., Eckstein, J., Frank, F., Garny, H., Gottschaldt, K.-D., Graf, P., Grewe, V., Kerkweg, A., Kern, B., Matthes, S., Mertens, M., Meul, S., Neumaier, M., Nützel,

770   M., Oberländer-Hayn, S., Ruhnke, R., Runde, T., Sander, R., Scharffe, D., and Zahn, A.: Earth System Chemistry integrated Modelling (ESCiMo) with the Modular Earth Submodel System (MESSy) version 2.51, Geoscientific Model Development, 9, 1153–1200, https://doi.org/10.5194/gmd-9-1153-2016, https://gmd.copernicus.org/articles/9/1153/2016/, 2016.

Johnston, H.: Reduction of Stratospheric Ozone by Nitrogen Oxide Catalysts from Supersonic Transport Exhaust, Science, 173, 517–522, https://doi.org/10.1126/science.173.3996.517, http://www.science.org/doi/abs/10.1126/science.173.3996.517, publisher: American Association for the Advancement of Science, 1971.

Johnston, H. S., Kinnison, D. E., and Wuebbles, D. J.: Nitrogen oxides from high-altitude aircraft: An update of potential effects on ozone, Journal of Geophysical Research: Atmospheres, 94, 16 351–16 363, https://doi.org/https://doi.org/10.1029/JD094iD13p16351, https://agupubs.onlinelibrary.wiley.com/doi/abs/10.1029/JD094iD13p16351, 1989.

Kerkweg, A. and Jöckel, P.: The infrastructure MESSy submodels GRID (v1.0) and IMPORT (v1.0), Geoscientific Model Development Discussions, 8, 8607–8633, https://doi.org/10.5194/gmdd-8-8607-2015, https://gmd.copernicus.org/preprints/8/8607/2015/, 2015.

Kerkweg, A., Buchholz, J., Ganzeveld, L., Pozzer, A., Tost, H., and Jöckel, P.: Technical Note: An implementation of the dry removal processes DRY DEPosition and SEDImentation in the Modular Earth Submodel System (MESSy), Atmospheric Chemistry and Physics, 6, 4617–4632, https://doi.org/10.5194/acp-6-4617-2006, https://acp.copernicus.org/articles/6/4617/2006/, 2006a.

Kerkweg, A., Sander, R., Tost, H., and Jöckel, P.: Technical note: Implementation of prescribed (OFFLEM), calculated (ONLEM), and pseudo-emissions (TNUDGE) of chemical species in the Modular Earth Submodel System (MESSy), Atmospheric Chemistry and Physics, 6, 3603–3609, https://doi.org/10.5194/acp-6-3603-2006, https://acp.copernicus.org/articles/6/3603/2006/, 2006b.

Kinnison, D., Brasseur, G. P., Baughcum, S. L., Zhang, J., and Wuebbles, D.: The Impact on the Ozone Layer of a Potential Fleet of Civil Hypersonic Aircraft, Earth's Future, 8, e2020EF001 626, https://doi.org/https://doi.org/10.1029/2020EF001626, https://agupubs.onlinelibrary.wiley.com/doi/abs/10.1029/2020EF001626, e2020EF001626 2020EF001626, 2020.

790   Lacis, A. A., Wuebbles, D. J., and Logan, J. A.: Radiative forcing of climate by changes in the vertical distribution of ozone, Journal of Geophysical Research: Atmospheres, 95, 9971–9981, https://doi.org/https://doi.org/10.1029/JD095iD07p09971, https://agupubs.onlinelibrary.wiley.com/doi/abs/10.1029/JD095iD07p09971, 1990.

le Texier, H., Solomon, S., and Garcia, R. R.: The role of molecular hydrogen and methane oxidation in the water vapour budget of the stratosphere, Quarterly Journal of the Royal Meteorological Society, 114, 281–295, https://doi.org/10.1002/qj.49711448002, https://onlinelibrary.wiley.com/doi/10.1002/qj.49711448002, 1988.

Lee, D., Fahey, D., Skowron, A., Allen, M., Burkhardt, U., Chen, Q., Doherty, S., Freeman, S., Forster, P., Fuglestvedt, J., Gettelman, A., De León, R., Lim, L., Lund, M., Millar, R., Owen, B., Penner, J., Pitari, G., Prather, M., Sausen, R., and Wilcox, L.: The contribution of global aviation to anthropogenic climate forcing for 2000 to 2018, Atmospheric Environment, 244, 117 834, https://doi.org/https://doi.org/10.1016/j.atmosenv.2020.117834, https://www.sciencedirect.com/science/article/pii/S1352231020305689, 2021.

Matthes, S., Lee, D. S., De Leon, R. R., Lim, L., Owen, B., Skowron, A., Thor, R. N., and Terrenoire, E.: Review: The Effects of Supersonic Aviation on Ozone and Climate, Aerospace, 9, https://doi.org/10.3390/aerospace9010041, https://www.mdpi.com/2226-4310/9/1/41, 2022.

Myhre, G., Kvalevåg, M., Raedel, G., Cook, J., Shine, K. P., Clark, H., Karcher, F., Markowicz, K., Kardas, A., Wolkenberg, P., et al.: Intercomparison of radiative forcing calculations of stratospheric water vapour and contrails, Meteorologische Zeitschrift, 18, 585, 2009.

Neis, P., Smit, H. G. J., Rohs, S., Bundke, U., Krämer, M., Spelten, N., Ebert, V., Buchholz, B., Thomas, K., and Petzold, A.: Quality assessment of MOZAIC and IAGOS capacitive hygrometers: insights from airborne field studies, Tellus B, 67, https://doi.org/10.3402/tellusb.v67.28320, 2015.

Noël, S., Weigel, K., Bramstedt, K., Rozanov, A., Weber, M., Bovensmann, H., and Burrows, J. P.: Water vapour and methane coupling in the stratosphere observed using SCIAMACHY solar occultation measurements, Atmospheric Chemistry and Physics, 18, 4463–4476, https://doi.org/10.5194/acp-18-4463-2018, https://acp.copernicus.org/articles/18/4463/2018/, 2018.

Peschka, W.: Hydrogen: The future cryofuel in internal combustion engines, International Journal of Hydrogen Energy, 23, 27–43, https://doi.org/https://doi.org/10.1016/S0360-3199(97)00015-3, https://www.sciencedirect.com/science/article/pii/S0360319997000153, 1998.

Petzold, A., Thouret, V., Gerbig, C., Zahn, A., Brenninkmeijer, C., Gallagher, M., Hermann, M., Pontaud, M., Ziereis, H., Boulanger, D., Marshall, J., Nédélec, P., Smit, H., Friess, U., Flaud, J.-M., Wahner, A., Cammas, J.-P., and Volz-Thomas, A.: Global-scale atmosphere monitoring by in-service aircraft - current achievements and future prospects of the European Research Infrastructure IAGOS, Tellus B, 67, https://doi.org/10.3402/tellusb.v67.28452, 2015.

Ponater, M., Pechtl, S., Sausen, R., Schumann, U., and Hüttig, G.: Potential of the cryoplane technology to reduce aircraft climate impact: A state-of-the-art assessment, Atmospheric Environment, 40, 6928–6944, https://doi.org/https://doi.org/10.1016/j.atmosenv.2006.06.036, https://www.sciencedirect.com/science/article/pii/S1352231006006686, 2006.

Pozzer, A., Jöckel, P., Sander, R., Williams, J., Ganzeveld, L., and Lelieveld, J.: Technical Note: The MESSy-submodel AIRSEA calculating the air-sea exchange of chemical species, Atmospheric Chemistry and Physics, 6, 5435–5444, https://doi.org/10.5194/acp-6-5435-2006, https://acp.copernicus.org/articles/6/5435/2006/, 2006.

Riese, M., Ploeger, F., Rap, A., Vogel, B., Konopka, P., Dameris, M., and Forster, P.: Impact of uncertainties in atmospheric mixing on simulated UTLS composition and related radiative effects, Journal of Geophysical Research: Atmospheres, 117, https://doi.org/10.1029/2012JD017751, http://onlinelibrary.wiley.com/doi/abs/10.1029/2012JD017751, _eprint: https://agupubs.onlinelibrary.wiley.com/doi/pdf/10.1029/2012JD017751, 2012.

Roeckner, E., Brokopf, R., Esch, M., Giorgetta, M., Hagemann, S., Kornblueh, L., Manzini, E., Schlese, U., and Schulzweida, U.: Sensitivity of Simulated Climate to Horizontal and Vertical Resolution in the ECHAM5 Atmosphere Model, Journal of Climate, 19, 3771 – 3791, https://doi.org/10.1175/JCLI3824.1, https://journals.ametsoc.org/view/journals/clim/19/16/jcli3824.1.xml, 2006.

Sander, R., Kerkweg, A., Jöckel, P., and Lelieveld, J.: Technical note: The new comprehensive atmospheric chemistry module MECCA, Atmospheric Chemistry and Physics, 5, 445–450, https://doi.org/10.5194/acp-5-445-2005, https://acp.copernicus.org/articles/5/445/2005/, 2005.

Sander, R., Baumgaertner, A., Gromov, S., Harder, H., Jöckel, P., Kerkweg, A., Kubistin, D., Regelin, E., Riede, H., Sandu, A., Taraborrelli, D., Tost, H., and Xie, Z.-Q.: The atmospheric chemistry box model CAABA/MECCA-3.0, Geoscientific Model Development, 4, 373–380, https://doi.org/10.5194/gmd-4-373-2011, https://gmd.copernicus.org/articles/4/373/2011/, 2011.

Scherrer, D., Dessornes, O., Ferrier, M., Vincent-Randonnier, A., Moule, Y., and Sabel'nikov, V.: Research on Supersonic Combustion and Scramjet Combustors at ONERA, AerospaceLab Journal, Issue 11, 20 pages, https://doi.org/10.12762/2016.AL11-04, https://aerospacelab.onera.fr/sites/www.aerospacelab-journal.org/files/AL11-04.pdf, artwork Size: 20 pages Medium: PDF Publisher: ONERA, 2016.

Shepherd, T. G. and McLandress, C.: A Robust Mechanism for Strengthening of the Brewer–Dobson Circulation in Response to Climate Change: Critical-Layer Control of Subtropical Wave Breaking, Journal of the Atmospheric Sciences, 68, 784–

797, https://doi.org/10.1175/2010JAS3608.1, http://journals.ametsoc.org/view/journals/atsc/68/4/2010jas3608.1.xml, publisher: American Meteorological Society Section: Journal of the Atmospheric Sciences, 2011.

Smit, H. G. J., Rohs, S., Neis, P., Boulanger, D., Krämer, M., Wahner, A., and Petzold, A.: Technical Note: Reanalysis of upper troposphere humidity data from the MOZAIC programme for the period 1994 to 2009, Atmos. Chem. Phys., 14, 13 241–13 255, https://doi.org/10.5194/acp-14-13241-2014, 2014.

Solomon, S., Garcia, R. R., and Stordal, F.: Transport processes and ozone perturbations, Journal of Geophysical Research: Atmospheres, 90, 12 981–12 989, https://doi.org/https://doi.org/10.1029/JD090iD07p12981, https://agupubs.onlinelibrary.wiley.com/doi/abs/10.1029/JD090iD07p12981, 1985.

Steelant, J. and Langener, T.: The LAPCAT-MR2 hypersonic cruiser concept, https://citeseerx.ist.psu.edu/viewdoc/download?doi=10.1.1.470.3649&rep=rep1&type=pdf, 2014.

Steelant, J., Varvill, R., Walton, C., Defoort, S., Hannemann, K., and Marini, M.: Achievements Obtained for Sustained Hypersonic Flight within the LAPCAT-II project, 20th AIAA International Space Planes and Hypersonic Systems and Technologies Conference, https://doi.org/10.2514/6.2015-3677, https://arc.aiaa.org/doi/abs/10.2514/6.2015-3677, 2015.

Stenke, A. and Grewe, V.: Simulation of stratospheric water vapor trends: impact on stratospheric ozone chemistry, Atmospheric Chemistry and Physics, 5, 1257–1272, https://doi.org/10.5194/acp-5-1257-2005, https://acp.copernicus.org/articles/5/1257/2005/, 2005.

Tegtmeier, S., Hegglin, M. I., Anderson, J., Bourassa, A., Brohede, S., Degenstein, D., Froidevaux, L., Fuller, R., Funke, B., Gille, J., Jones, A., Kasai, Y., Krüger, K., Kyrölä, E., Lingenfelser, G., Lumpe, J., Nardi, B., Neu, J., Pendlebury, D., Remsberg, E., Rozanov, A., Smith, L., Toohey, M., Urban, J., von Clarmann, T., Walker, K. A., and Wang, R. H. J.: SPARC Data Initiative: A comparison of ozone climatologies from international satellite limb sounders, Journal of Geophysical Research: Atmospheres, 118, 12,229–12,247, https://doi.org/https://doi.org/10.1002/2013JD019877, https://agupubs.onlinelibrary.wiley.com/doi/abs/10.1002/2013JD019877, 2013.

Terrenoire, E., Hauglustaine, D. A., Gasser, T., and Penanhoat, O.: The contribution of carbon dioxide emissions from the aviation sector to future climate change, Environmental Research Letters, 14, 084 019, https://doi.org/10.1088/1748-9326/ab3086, https://doi.org/10.1088/1748-9326/ab3086, 2019.

Terrenoire, E., Hauglustaine, D., Cohen, Y., Cozic, A., Valorso, R., Lefèvre, F., and Matthes, S.: Impact of present and future aircraft NOx and aerosol emissions on atmospheric composition and associated direct radiative forcing of climate, Atmos. Chem. Phys, under review,, 2022.

Tost, H., Jöckel, P., Kerkweg, A., Sander, R., and Lelieveld, J.: Technical note: A new comprehensive SCAVenging submodel for global atmospheric chemistry modelling, Atmospheric Chemistry and Physics, 6, 565–574, https://doi.org/10.5194/acp-6-565-2006, https://acp.copernicus.org/articles/6/565/2006/, 2006.

Tost, H., Jöckel, P., and Lelieveld, J.: Lightning and convection parameterisations - uncertainties in global modelling, Atmospheric Chemistry and Physics, 7, 4553–4568, https://doi.org/10.5194/acp-7-4553-2007, https://acp.copernicus.org/articles/7/4553/2007/, 2007.

Tuck, A. F.: Perspective on aircraft in the stratosphere: 50 years from COMESA through the ozone hole to climate, Quarterly Journal of the Royal Meteorological Society, 147, 713–727, https://doi.org/https://doi.org/10.1002/qj.3958, https://rmets.onlinelibrary.wiley.com/doi/abs/10.1002/qj.3958, 2021.

UN: https://unfccc.int/process-and-meetings/the-paris-agreement/the-paris-agreement, 2015.

Viola, N., Fusaro, R., Ferretto, D., Gori, O., Saracoglu, B., Ispir, A. C., Grewe, V., Plezer, J. F., Martinez, J., Marini, M., Cutrone, L., Hernandez, S., Lammers, K., Vincent, A., Hauglustaine, D., Linke, F., Bodmer, D., Nilsson, T., and Fureby, C.: H2020 STRATOFLY

Project: From Europe To Australia in less than three hours, Congress of the International Council of the Aeronautical Sciences, p. 21, 2021a.

Viola, N., Fusaro, R., Gori, O., Marini, M., Roncioni, P., Saccone, G., Saracoglu, B., Ispir, A. C., Fureby, C., Nilson, T., Iron, C., Vincent, A., Martinez Schramm, J., Grewe, V., Emmerig, J., Hauglustaine, D., Linke, F., and Bodmer, D.: STRATOFLY MR3 – how to reduce the environmental impact of high-speed transportation, in: AIAA Scitech 2021 Forum, American Institute of Aeronautics and Astronautics, https://doi.org/10.2514/6.2021-1877, https://arc.aiaa.org/doi/10.2514/6.2021-1877, 2021b.

Visualization and Analysis Systems Technologies: Geoscience Community Analysis Toolkit (GeoCAT-comp) [Software], https://doi.org/10.5065/a8pp-4358, 2021.

Winterstein, F. and Jöckel, P.: Methane chemistry in a nutshell – the new submodels CH4 (v1.0) and TRSYNC (v1.0) in MESSy (v2.54.0), Geoscientific Model Development, 14, 661–674, https://doi.org/10.5194/gmd-14-661-2021, https://gmd.copernicus.org/articles/14/661/2021/, 2021.

Zhang, J., Wuebbles, D., Kinnison, D., and Baughcum, S. L.: Potential Impacts of Supersonic Aircraft Emissions on Ozone and Resulting Forcing on Climate: An Update on Historical Analysis, Journal of Geophysical Research: Atmospheres, n/a, e2020JD034130, https://doi.org/https://doi.org/10.1029/2020JD034130, https://agupubs.onlinelibrary.wiley.com/doi/abs/10.1029/2020JD034130, e2020JD034130 2020JD034130, 2021.

Appendix A

The applied EMAC model setup comprised the submodels AEROPT (AERosol OPTical properties), AIRSEA, CH4, CLOUD, CLOUDOPT (CLOUD OPTical properties), CONTRAIL, CONVECT (CONVECTion), CVTRANS (Convective Tracer TRANS-port), DRADON (Decay RADioactive ONline), DDEP, E5VDIFF (ECHAM5 Vertical DIFFusion), GWAVE (Gravity WAVE), H2OEMIS, JVAL (J VALues), LNOX, MECCA, MSBM, O3ORIG (O3 ORIGin), OFFEMIS, ONEMIS, ORBIT, OROGW (OROgraphic Gravity Waves), PTRAC (Passive TRACers), QBO (Quasi Biannual Oscillation), RAD (RADiation), S4D (Sampling in 4 Dimensions), SATSIMS (Satellites Simulator), SCALC (Simple CALCulations), SCAV, SCOUT (Stationary Column OUTput), SEDI, SORBIT (Satellite ORBITs), SURFACE, TBUDGET, TENDENCY, TNUDGE (Tracer NUDG(E)ing), TR-EXP (Tracer Release EXperiments from Point sources), TROPOP (TROPOPause) and VISO (Vertically layered iso-surfaces and maps) (Jöckel et al., 2006, 2010; Roeckner et al., 2006). Further information is available on the MESSy homepage https://www.messy-interface.org/.

Table A1. Short- and longwave contributions to radiative forcing in $\mathrm{mWm^{-2}}$ for EMAC, including upper tropospheric perturbation of water vapour, ozone and methane, and the related error potential of approximately 51 to 63 % due to the integration of tropospheric perturbations.

Aircraft	Perturbation	SW RF	LW RF	RF
ZEHST	H_2O	0.07	31.43	31.50
LAPCAT	H_2O	-0.44	56.18	55.74

Table A2. Change in global methane lifetime for LMDZ-INCA and EMAC and the ZEHST and LAPCAT scenarios.

Scenario	EMAC	LMDZ-INCA
ZEHST	-0.03 %	-0.09 %
LAPCAT	-0.09 %	-0.16 %
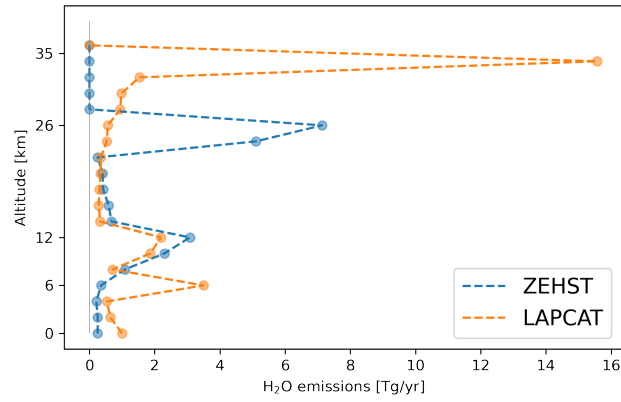
Figure A1. Vertical distribution of annual H_2O emission for ZEHST and LAPCAT. The peak at 6 km altitude comes from hypersonic boost of the LAPCAT aircraft. The vertical distribution was aggregated for a better comparability (with a 2 km bin size). For the total amount of emission, see Table 2.
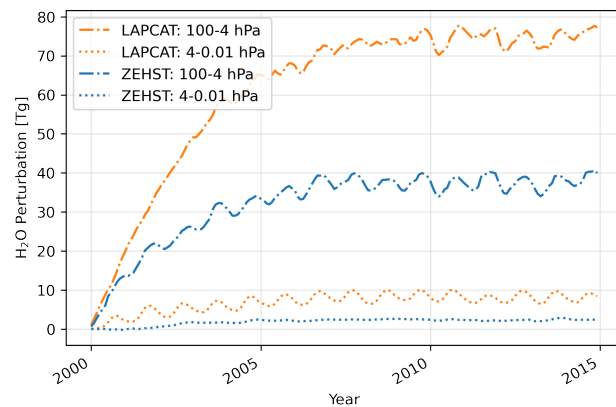
Figure A2. Timeline plot of accumulated trace gas H_2O in teragram, based on monthly mean values. Blue lines represent scenario ZEHST and orange lines represent scenario LAPCAT. Shown is the H_2O perturbation over time above 4 hPa (dotted) and from 4-100 hPa (solid-dotted).
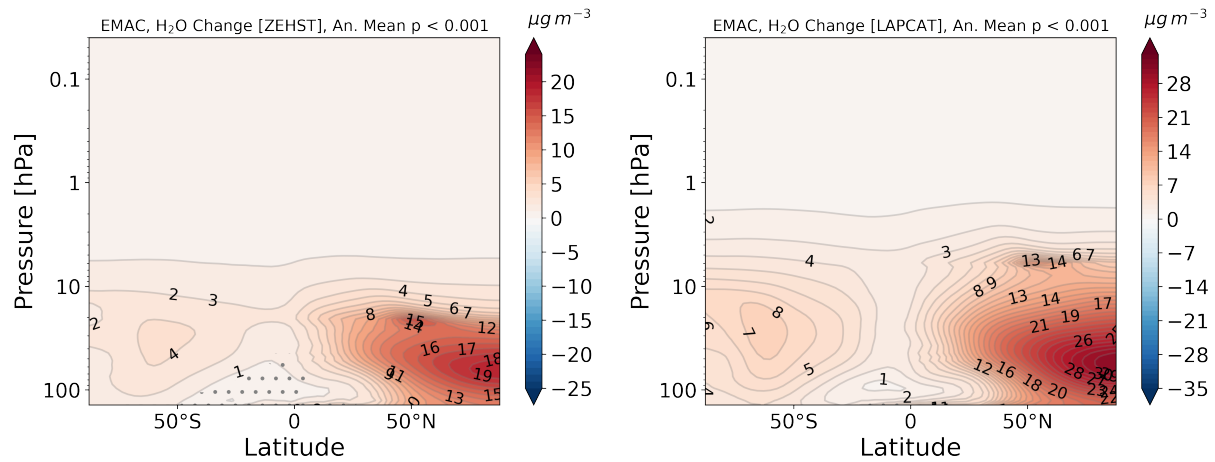
Figure A3. Multi-annual mean (2010-2014) of H_2O-perturbation [$\mu g\,m^{-3}$] for the ZEHST scenario (a) and the LAPCAT scenario (b). Dotted areas represent probabilities larger than 0.1 % for data not to be significant (standard t-test). Horizontal lines represent respective cruise altitudes.
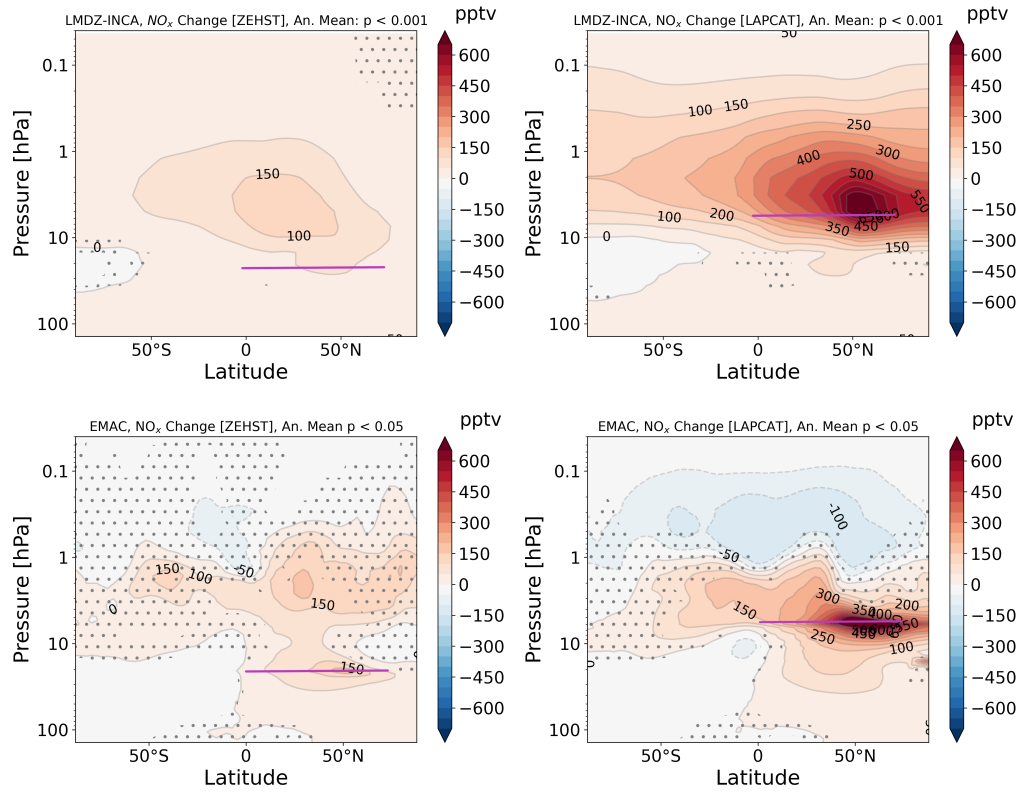
Figure A4. Annual mean (2010-2014) of NO_x perturbation (pptv) for the ZEHST scenario (left) and the LAPCAT scenario (right) for both models LMDZ-INCA (top) and EMAC (bottom). Purple lines represent respective cruise altitudes. Hatched areas are characterized by a p-value higher than the threshold indicated in the title of each plot.
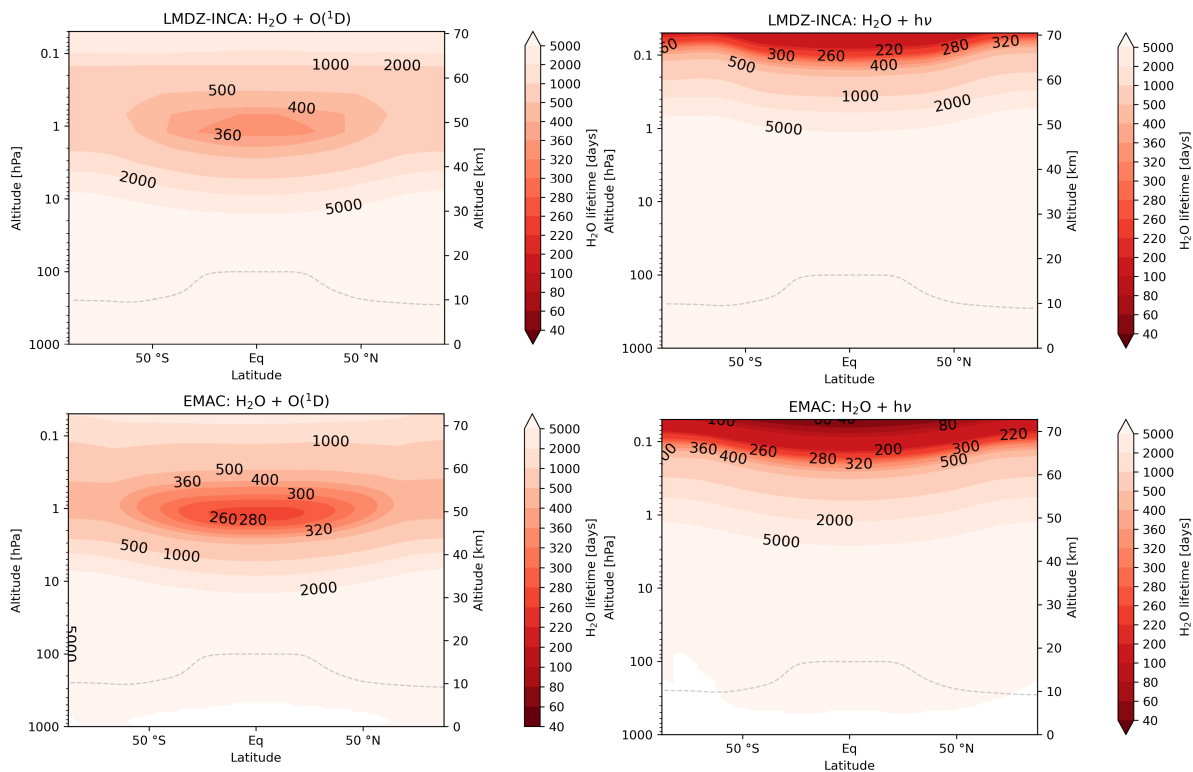
Figure A5. Zonal mean (photo-)chemical H_2O lifetime in days for photolysis (right column) and reaction with $O(^1D)$ (left column) for LMDZ-INCA (upper row) and EMAC (lower row).
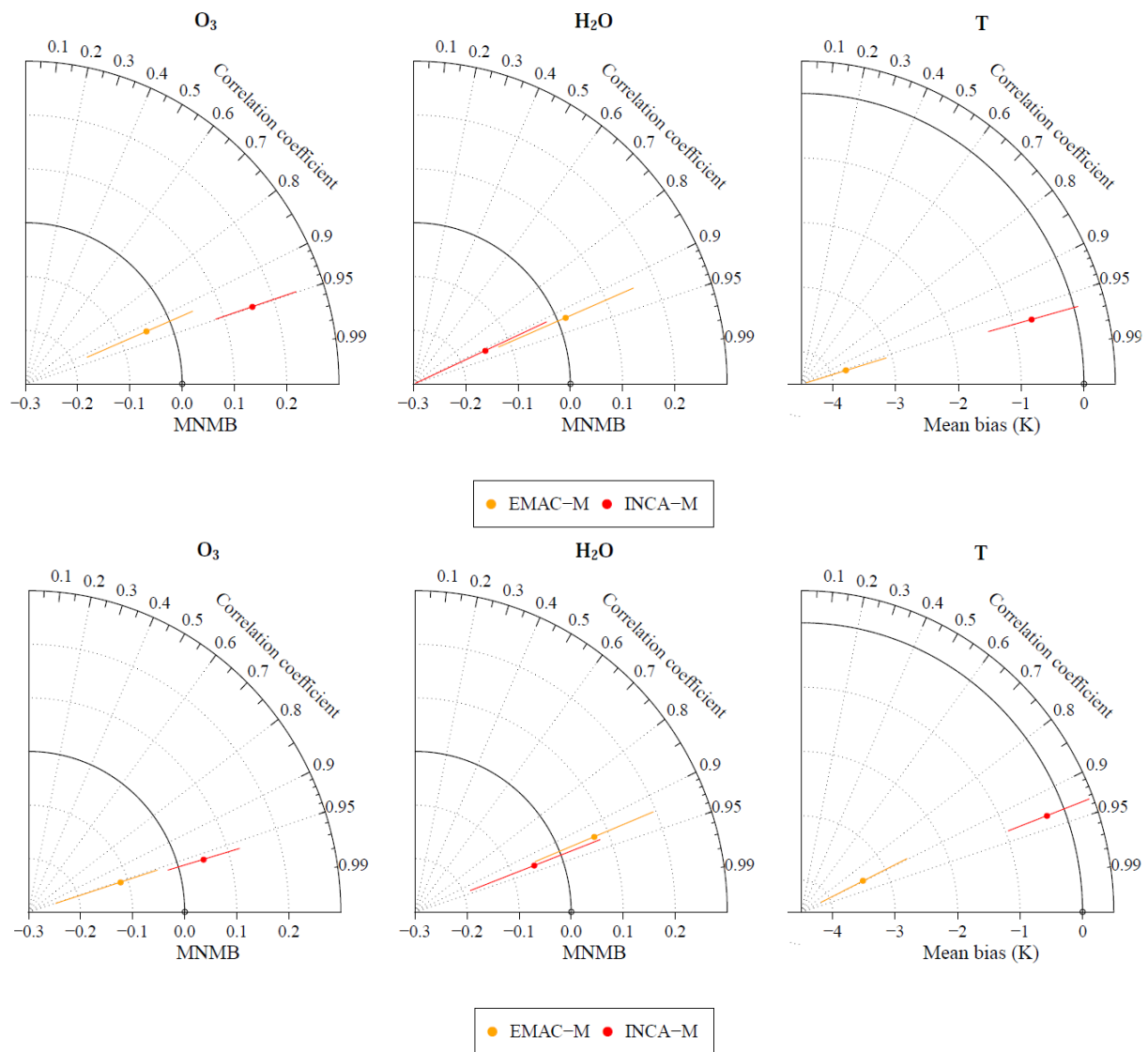
Figure A6. Same as Fig. 4 for winter (first row) and spring (second row).
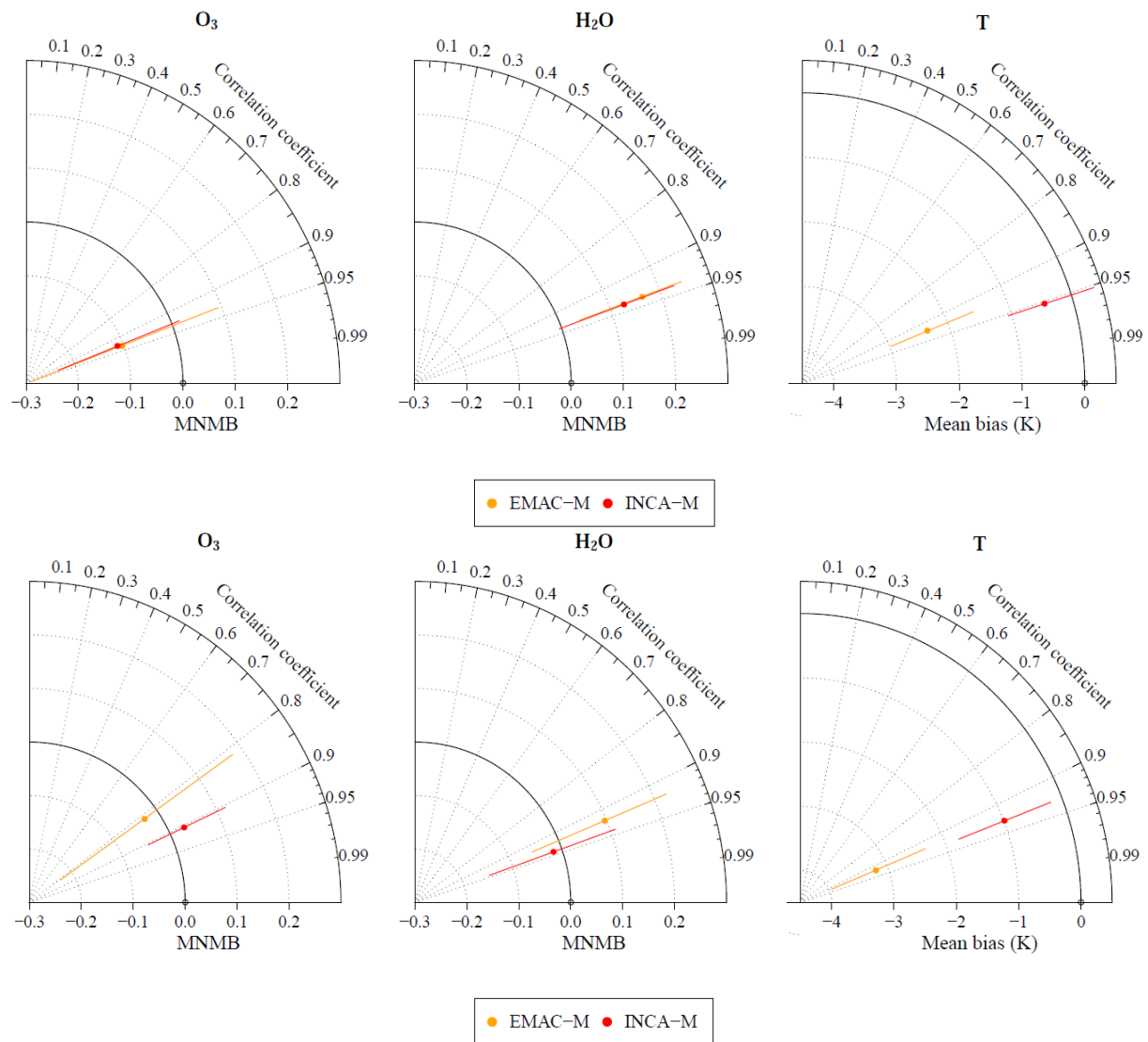
Figure A7. Same as Fig. 4 for summer (first row) and autumn (second row).
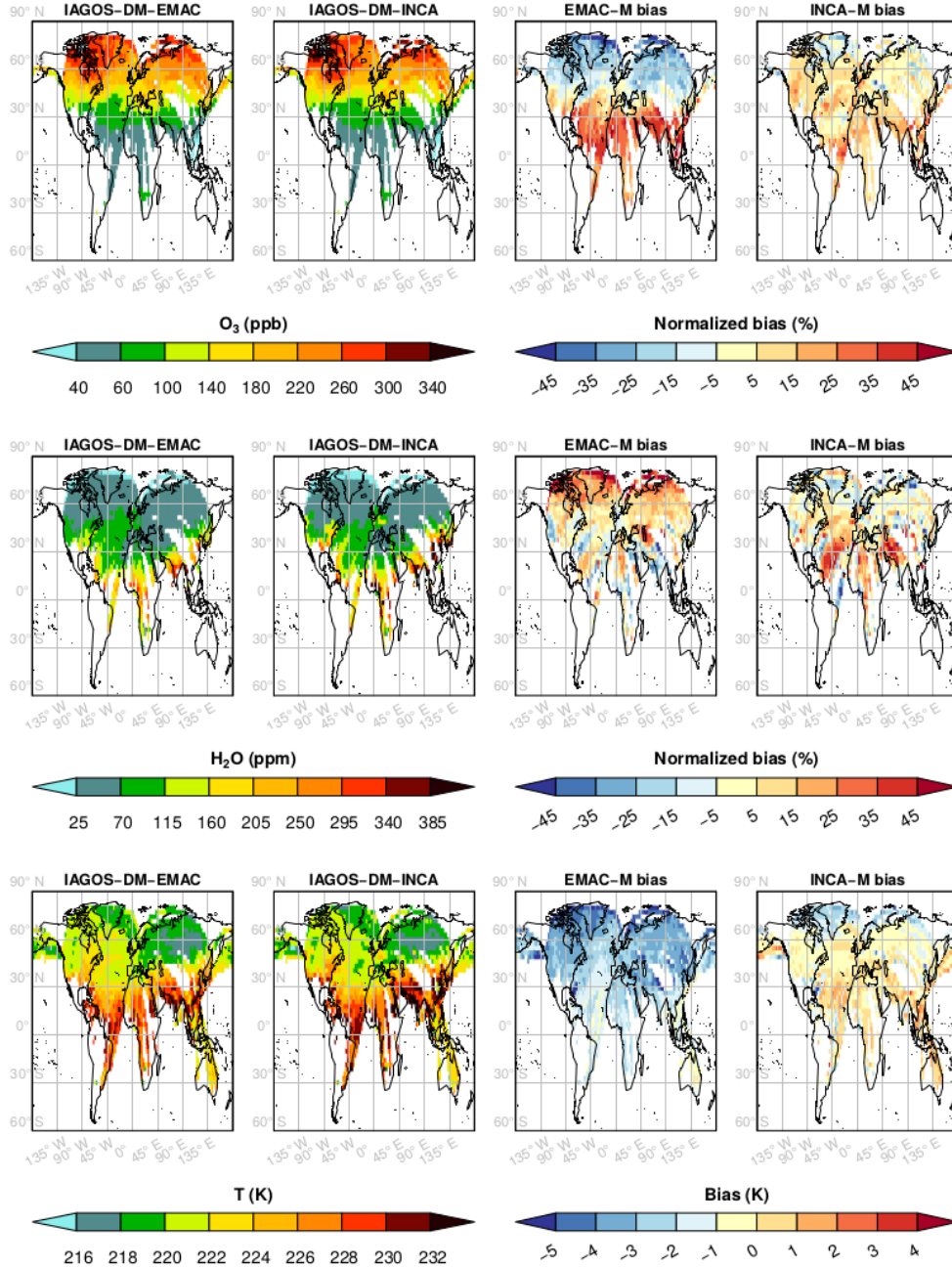
Figure A8. Annual mean climatologies for ozone, water vapour and temperature (from top to bottom) averaged over 2000–2014, and vertically through the cruise levels. The first and second columns represent the climatologies seen by the IAGOS observations, projected onto the EMAC grid and onto the INCA grid respectively, the latter being interpolated onto the EMAC grid afterward. The third and fourth columns show the biases between the reference simulation for each model and its corresponding gridded IAGOS product. For each grid cell, the normalized bias for the mixing ratios is calculated relatively to the average between observations and the model simulation.

DJF
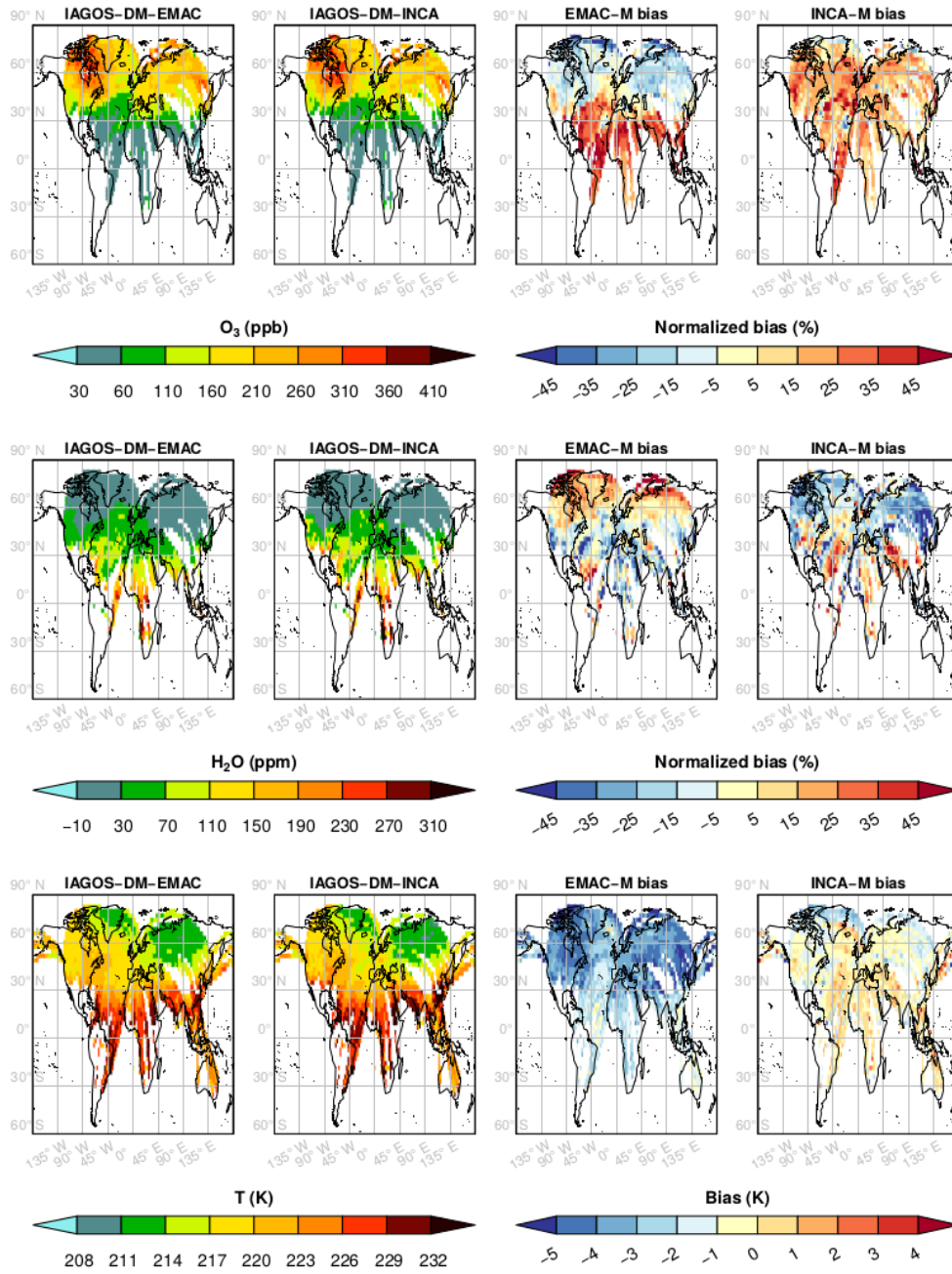
Figure A9. Same as Fig. A8 for boreal winter.

MAM
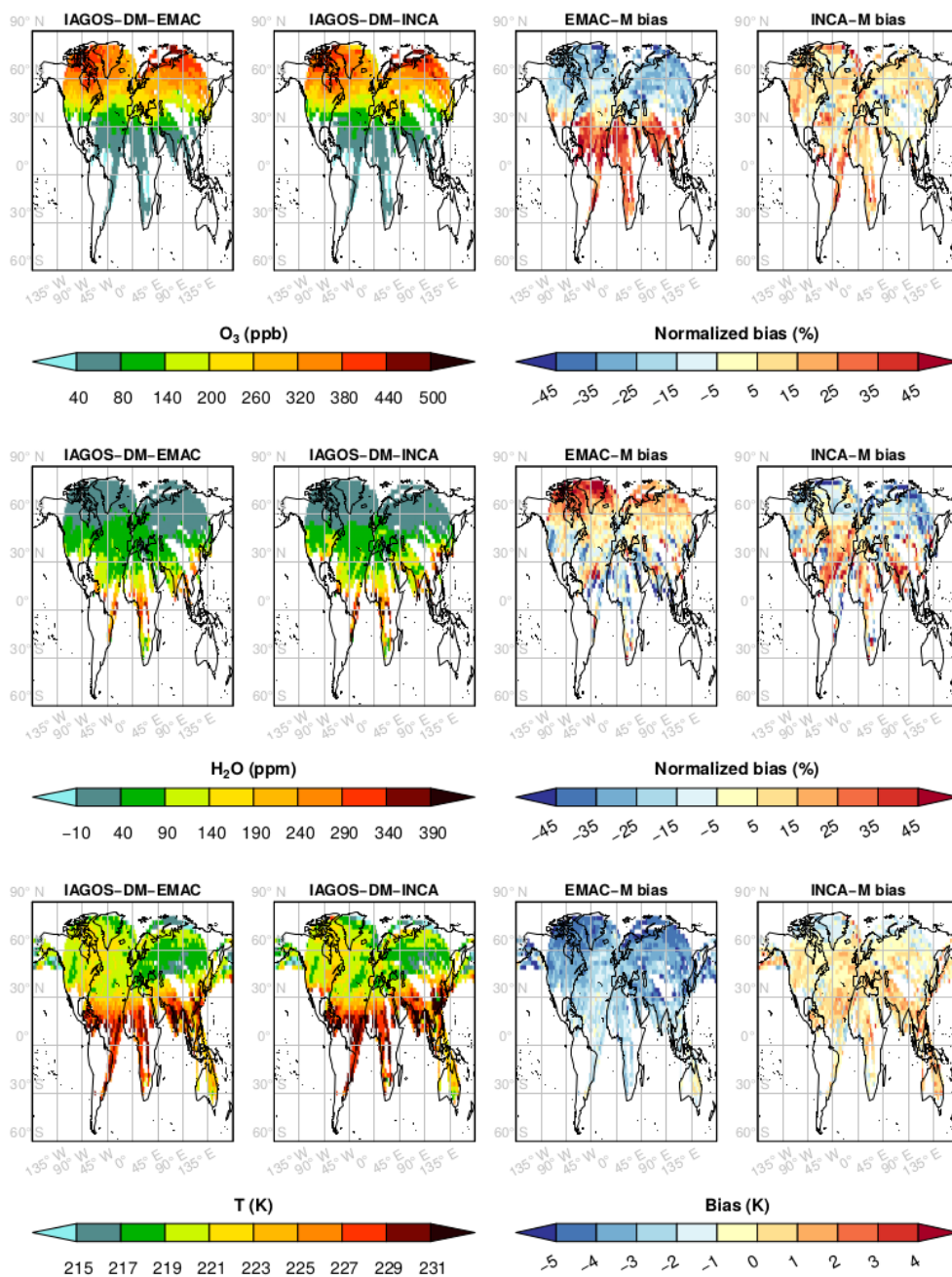
Figure A10. Same as Fig. A8 for boreal spring.

JJA
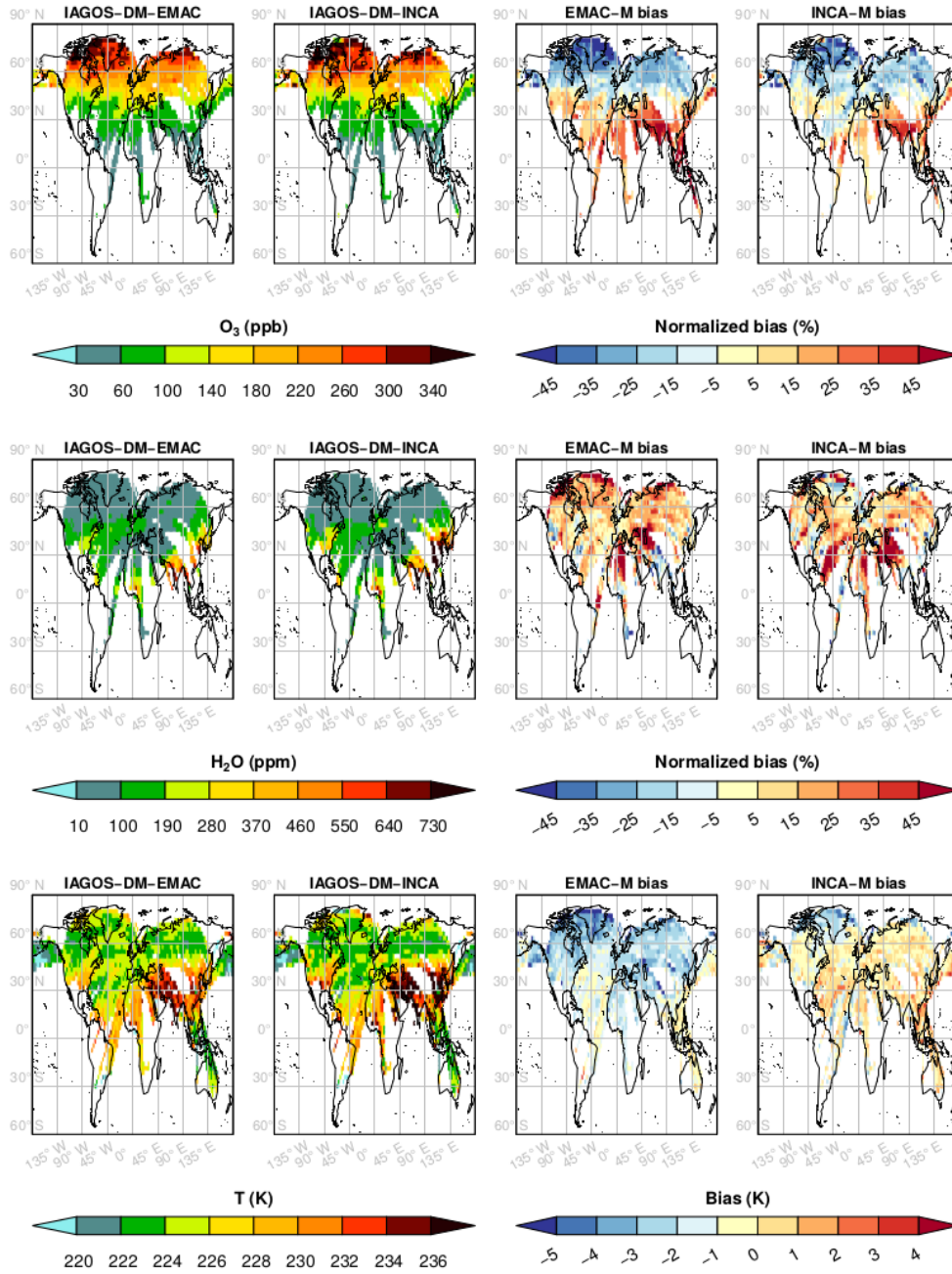
Figure A11. Same as Fig. A8 for boreal summer.

SON
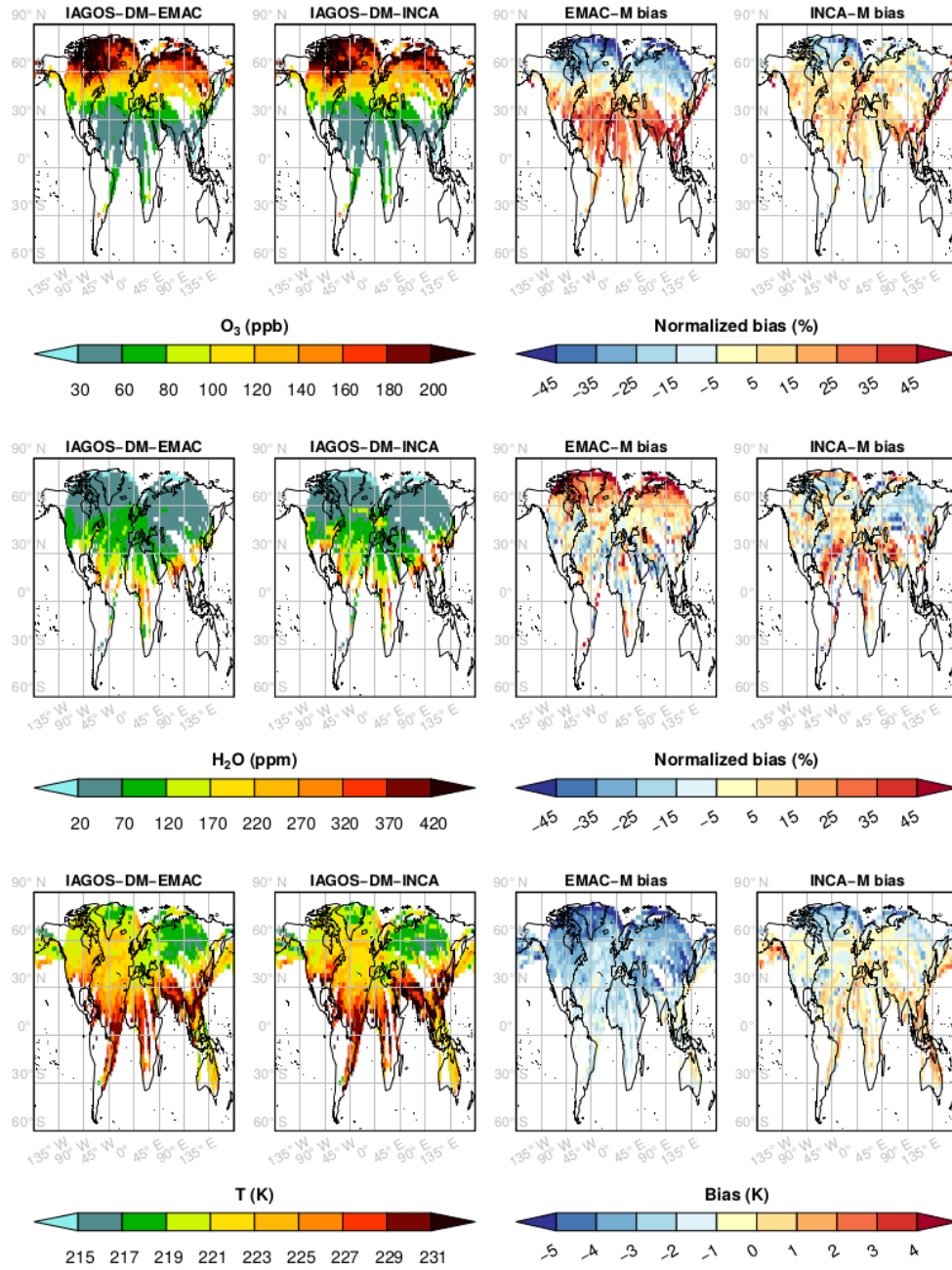
Figure A12. Same as Fig. A8 for boreal autumn.

Code availability

The Modular Earth Submodel System (MESSy) is continuously further developed and applied by a consortium of institutions. The usage of MESSy and access to the source code is licenced to all affiliates of institutions which are members of the

910 MESSy Consortium. Institutions can become a member of the MESSy Consortium by signing the MESSy Memorandum of Understanding. More information can be found on the MESSy Consortium Website (http://www.messy-interface.org). The submodel H2OEMIS (water vapour emissions) presented here has been implemented in MESSy version 2.54.0 and is available in the official release 2.55.0. The LMDZ-INCA global model is part of the Institut Pierre Simon Laplace (IPSL) Climate Modelling Center Coupled Model. The documentation on the code and the code itself can be found at https://cmc.ipsl.fr/ipsl-

915 climate-models/ipsl-cm6/. The distribution of the IAGOS data onto the EMAC and LMDZ-INCA grids is based on an updated version of the Interpol-IAGOS software, available at https://doi.org/10.25326/81 (Cohen et al., 2021b).

Data availability

To access datasets of LMDZ-INCA results please contact Didier Hauglustaine. For access to datasets of EMAC results please contact Johannes Pletzer. The IAGOS data set can be found at http://doi.org/10.25326/20 (Petzold et al., 2015) and more

920 precisely, the IAGOS time series used in this study are available at http://doi.org/10.25326/06 (Bundke et al., 2018).

Video supplement. Two video supplements are published with a doi via zenodo.org. The first supplement shows the time development of SWV and integrated H_2O perturbation by LAPCAT aircraft at 32-38 km altitude (http://doi.org/10.5281/zenodo.4455592) over a time period of fifteen years (2000-2014). The second supplement shows the transport of H_2O emission by LAPCAT aircraft in the first month of airfleet operation at stratospheric altitudes. The presentation is a world map view (http://doi.org/10.5281/zenodo.4475334).

925 *Author contributions.* Johannes Pletzer set-up the EMAC model simulations, analysed and post-processed the EMAC model results. Didier Hauglustaine set-up the LMDZ-INCA model simulations, analysed and post-processed the LMDZ-INCA model results, which Johannes Pletzer plotted for a consistent presentation. Yann Cohen contributed with the IAGOS observation validation of both models. Patrick Jöckel helped with the choice of the initial EMAC setup and with the writing of the H2OEMIS submodel. Volker Grewe was involved in the discussion of the results and supported the writing of the document. The manuscript was written by Johannes Pletzer, then reviewed by the

930 authors and approved by all the authors.

Competing interests. The authors declare that they have no conflict of interest.

935

940

945

950